https://doi.org/10.5194/acp-2019-507
Preprint. Discussion started: 3 June 2019

Atmospheric Chemistry and Physics Discussions

Evidence of the complexity of aerosol transport in the lower troposphere on the Namibian coast during AEROCLO-sA

Patrick Chazette[1], Cyrille Flamant[2], Julien Totems[1], Marco Gaetani[2,3], Gwendoline Smith[1,3], Alexandre Baron[1], Xavier Landsheere[3], Karine Desboeufs[3], Jean-François Doussin[3], and Paola Formenti[3]

[1]Laboratoire des Sciences du Climat et de l'Environnement (LSCE), Laboratoire mixte CEA-CNRS-UVSQ, UMR CNRS 1572, CEA Saclay, 91191 Gif-sur-Yvette, France
[2]LATMOS/IPSL, Sorbonne Université, CNRS, UVSQ, Paris, France
[3] Laboratoire Interuniversitaire des Systèmes Atmosphériques (LISA) UMR CNRS 7583, Université Paris-Est-Créteil, Université de Paris, Institut Pierre Simon Laplace, Créteil, France.

Correspondence to: Patrick Chazette (patrick.chazette@lsce.ipsl.fr)

Abstract. The evolution of the vertical distribution and optical properties of aerosols in the free troposphere, above stratocumulus, is analysed for the first time over the Namibian coast, a region where uncertainties on aerosol-cloud coupling in climate simulations are significant. We show the high variability of atmospheric aerosol composition in the lower and middle troposphere during the AEROCLO-sA field campaign (22 August - 12 September 2017) around the Henties Bay supersite, using a combination of ground-based, airborne and space-borne lidar measurements. Three distinct periods of 4 to 7 days are observed, associated with increasing aerosol loads (aerosol optical thickness at 550 nm ranging from ~ 0.2 to ~0.7), as well as increasing aerosol layer depth and top altitude. Aerosols are observed up to 6 km above mean sea level during the later period. Aerosols transported within the free troposphere are mainly polluted dust (dust mixed with smoke from fires in Angola) for the first 2 periods (22 August-1 September 2017) and smoke (from Angola and South America) for the last part (3-9 September) of the field campaign. Lagrangian back trajectory analyses highlight that the highest aerosol layers (between 5 and 6 km above mean sea level) come from South America (Brazil, Argentina and Paraguay) and reach Henties Bay after 4 to 5 days. They are transported eastward by the mid latitude westerlies and towards Southern Africa by the equatorward moving cut-off low originating within the westerlies. This results in a very complex mixture of aerosols over the coastal regions of Namibia that must be taken into account when investigating aerosols radiative effects above stratocumulus clouds in the south east Atlantic Ocean.

Keywords: dust, biomass burning aerosols, regional transport, atmospheric dynamics, back trajectories, lidar

1 Introduction

The western coast of southern Africa is a complex area in terms of both atmospheric composition and dynamics, where aerosol-radiation-cloud interactions play a significant role on local and remote climates. A large part of this complexity is related to atmospheric circulation associated with a low-laying coastal strip next to an elevated continental plateau covering most of the sub-continent, as well as fast evolving synoptic patterns largely controlled by the S[t] Helena anticyclone over the Atlantic and the mid-latitude westerlies on the poleward edge of this high-pressure system (Tyson and Preston-White, 2000). The complexity inherent to the atmospheric composition over this region is also linked to the variety of aerosol sources and the way they are transported at the regional scale.

https://doi.org/10.5194/acp-2019-507
Preprint. Discussion started: 3 June 2019

Southern Africa is the most important source of biomass burning aerosols (BBA) while dust aerosol emission sources are found along the Namibian coast lines, as well as in the Etosha Pan in Namibia and in the Makgadikgadi Pan in Botswana (Ginoux et al., 2012; Vickery et al., 2013). Anthropogenic sources are related to industrial emissions from South Africa and port activities in Namibia, together with ship emissions (Johansson et al., 2017) along the Namibian coast, that give rise to elevated concentrations of sulfate aerosols. Finally, sea salt aerosols emitted over the south east Atlantic as a result of strong winds swirling around the S^t Helena anticyclone and sulphur species emissions over the northern Benguela Upwelling System of the coast of Namibia (Andreae et al., 2004; Bates et al., 2001) also contribute to the atmospheric composition over coastal southern Africa. Furthermore, the ocean region off the coast of Angola and Namibia is covered by a quasi-permanent stratocumulus deck, topping the marine boundary layer (Keil and Haywood, 2003). As a result, the air over the coastal region of southern Africa is not only a unique mixture of various gases as well as liquid and solid particles, it also presents a very layered structure, with marine aerosols, anthropogenic pollution and dust emitted along the coastline present in the marine boundary layer (i.e. below the stratocumulus deck) and BBA and dust emitted over the continental plateau being transported aloft. The stratification of the aerosol layers evolves over the south east Atlantic with the distance from the coastline as also mixes across the stratocumulus layer (Adebiyi and Zuidema, 2016; Gordon et al., 2018). These clouds being particularly sensitive to aerosol presence (e.g. Costantino and Bréon, 2013, 2010) and the most effective in reflecting solar radiation back to space, the coastal southern Africa region is arguably one of the regions where the aerosol-radiation-cloud interactions are strongest in the world (Adebiyi et al., 2015; Fuchs et al., 2017).

The vertical distribution of aerosols (and absorbing aerosols in particular) as well as their location with respect to bright low-level clouds (above or below) is of paramount importance as it significantly influences the vertical profile of radiative heating in the atmosphere (e.g. Léon et al., 2002; Ramanathan et al., 2007; Raut and Chazette, 2008) and, in turn, the stability of the atmosphere, thereby modifying convective and turbulent motions and clouds (e.g. Ackerman et al., 2000; McFarquhar and Wang, 2006). In this context, state-of-the-art climate models diverge by several W m^{-2} when attempting to calculate the regional direct radiative effect over coastal Southern Africa (Myhre et al., 2013; Stier et al., 2013) ranging from negative (-3 W m^{-2}) to strong positive forcing (+5 Wm^{-2}) for mean seasonal averages. This is mainly because of a limited knowledge of aerosol properties, vertical position of aerosol and cloud layers. These model shortcomings can also affect climate simulations in remote areas. Indeed, perturbations of the radiative budget in this area have been shown to be connected with rainfall anomalies in Brazil (Jones et al., 2009) or to influence the position of the Intertropical Convergence Zone and, in turn, the African and Asian monsoon (Jones and Haywood, 2012).

The main purpose of this article is to characterise the temporal and spatial evolutions of vertical distribution of aerosols optical properties observed along the coastline of Namibia, in Henties Bay, in August and September 2017 during the Aerosols, Radiation and Clouds in southern Africa (AEROCLO-sA) field campaign (Formenti et al., 2019). The evolution of the vertical distribution of aerosols properties is examined as a function of the synoptic conditions and aerosol source activation. The investigation is conducted by analysing a combination of ground-based, airborne and space-borne lidar measurements, together with back-trajectory and numerical weather forecast model analyses, as well as complementary space-borne passive sensors observations.

Section 2 presents the observations and provides a description of the ground-based, airborne and space-borne active and passive remote sensing instruments used during the field campaign, together with complementary numerical simulation tools. Section 3 presents the evolution of the vertical profiles of aerosols during the

https://doi.org/10.5194/acp-2019-507
Preprint. Discussion started: 3 June 2019

campaign, together with the main optical and geometrical characteristics of the lifted aerosol layers and identifies three distinct periods with increasing aerosol load. The variability of the vertical distribution of aerosols around Henties Bay during the later period is assessed using lidar and dropsonde measurements acquired over the ocean, as detailed in Section 4. In Section 5, we investigate the different origins and transport pathways of aerosols in the free troposphere towards Henties Bay during the 3 periods. The last section is dedicated to the summary and conclusion. The description of the ground-based lidar is given in Appendix A, together with the calibration and data inversion processing.

2 Observations and simulations

The AEROCLO-sA supersite of Henties Bay (-22° 6’ S, 14° 17’ E, Figure 1) belongs to the Sam Nujoma Marine and Coastal Resources Research Centre (SANUMARC) of the University of Namibia in the Orongo region. It has been selected because of its geographical position: bounded by the Atlantic Ocean on its western side and by the Namibia desert, ~800 m above the mean sea level (AMSL), on its eastern side (Formenti et al., 2019). The analysis presented here relies mainly on active and passive remote sensing observations acquired from i) ground-based instruments deployed in Henties Bay, namely an ALS 300 lidar (Leosphere Inc, Saclay, France) operating at a wavelength of 355 nm and a sun photometer from the National Aeronautics and Space Administration Aerosol Robotic Network (AERONET), ii) the airborne lidar LEANDRE nouvelle Génération (LNG) installed on the Service des Avions Français Instrumentés pour la Recherche en Environnement (SAFIRE) Falcon 20 which flew several times in the vicinity of Henties Bay and iii) space-borne instruments, namely the Cloud-Aerosol Lidar with Orthogonal Polarization (CALIOP), the Cloud-Aerosol Transport System (CATS) lidar and the Moderate-Resolution Imaging Spectroradiometer (MODIS). The available measurements are given in Table 1 against both the date and the universal time count (UTC). The synergy between ground-based lidar measurements, space-borne observations (aerosol typing and aerosol optical thickness (AOT)) and those of the sun photometer (AOT and Ångström exponent) was used to better constrain the retrieval of the aerosol optical parameters (see Appendix A): aerosol extinction coefficient (AEC), lidar ratio (LR) and particle depolarisation ratio (PDR). The space-borne lidar-derived aerosol types are associated with prescribed LRs (see Section 2.4) that are used for the inversion of the ground-based lidar.

Table 1: Data available during the field campaign on August and September 2017 from: the ground-based ALS lidar and AERONET sun photometer in Henties Bay, the airborne LNG lidar, dropsonde released from the Falcon 20, as well as the CATS and CALIOP space-borne lidars. The line highlighted in bold indicates when the AERONET inversion allows the retrieval of a relevant value for the lidar ratio (level 2 data). The aerosol typing as provided by CALIOP and CATS is also indicated for overpasses in the vicinity of Henties Bay.

Date	ALS measurement time (UTC)	F20 flight LNG & dropsonde measurement time (UTC)	**Coupling ALS/ AERONET**	**CALIOP** Orbit close to the site	**CATS Overpass time (UTC)**
22 Aug	1400-2400	-	X	-	-

https://doi.org/10.5194/acp-2019-507
Preprint. Discussion started: 3 June 2019

23 Aug	1645-2330	-	X	-	0342-0357 Smoke
27 Aug	1545-1700	-	X	-	-
28 Aug	1030-1230	-	X	10.2017-08-28T00-08-17ZN 10.2017-08-28T12-26-48ZD Polluted dust/Smoke	-
29 Aug	1730-2250	-	-	10.2017-08-29T23-55-43ZN Smoke	0122-0207 Smoke
30 Aug	1800-2000	-	-		0047-0102 Smoke
31 Aug	1430-2100	-	X	10.2017-08-31T12-57-28ZD Smoke/Polluted dust	1452-1507 Smoke/Dust
02 Sep	0930-1130 1715-1900	-	X	10.2017-09-02T12-44-54ZD Smoke/Polluted dust	-
03 Sep	**1400-1540**	**-**	**X**	-	-
04 Sep	2330-2400	-	-	10.2017-09-04T00-13-44ZN Smoke	-
05 Sep	1400-1500 1845-1945	Flight 6 LNG: ~1000 Dropsonde #5: 0952	-	-	2204-2219 Smoke
06 Sep	0100-0200 0830-1230	Flight 8 LNG: ~0830 and ~0900 Dropsondes #3 and #4: 0843 and 0908	X	-	1258-1313 Smoke/dust

https://doi.org/10.5194/acp-2019-507
Preprint. Discussion started: 3 June 2019

Atmospheric Chemistry and Physics Discussions

07 Sep	1600-2100	-	-	-	2156-2211 Smoke
08 Sep	1300-1500 2000-2200	-	-	-	2052-2107 Smoke
09 Sep	0000-0045 0900-1200	-	X	-	2001-2016 Smoke

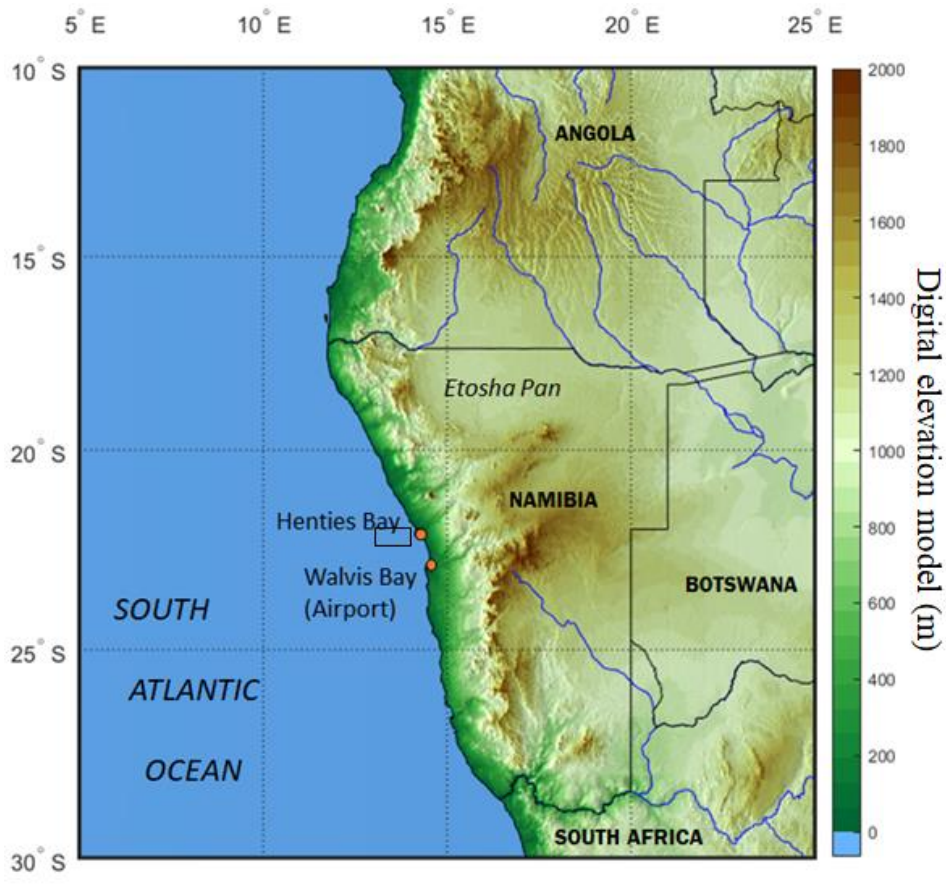

Figure 1: Location of the Henties Bay experimental site (in Namibia) on the west African coast. The Walvis Bay airport where the SAFIRE Falcon 20 aircraft operated during AEROCLO-sA is also indicated. The black rectangle surrounds the area chosen to average the MODIS-derived AOTs.

2.1 Ground-based lidar

The ALS lidar measurements were carried out continuously between 22 August and 13 September, 2017. For the aerosol study there is much less data during clear sky because of the quasi-ubiquitous presence of marine stratocumulus and fog during a large part of the observation days. The fog opacity is often such that the laser beam is fully attenuated after a few hundred meters. We therefore considered average profiles taken during periods when no low-level clouds or fog events are observed, i.e. between about 1 and 4 hours on a given day (see Table 1). The description of the lidar is given in Appendix A, together with the calibration and data inversion processing.

2.2 AERONET sun photometer

The site of Henties Bay was equipped with a sun and sky scanning spectral radiometer manufactured by CIMEL Inc (Paris, France) and belonging to the AERONET automatic and global network of sun photometers providing long-term and continuous monitoring of aerosol optical, microphysical and radiative properties (http://aeronet.gsfc.nasa.gov/). Eight spectral bands are generally used between 340 and 1020 nm. The aerosol optical thickness at the lidar wavelength of 355 nm (AOT_{355}) is assessed using the Ångström exponent (Ångström, 1964) and the sun photometer AOT at 380 and 440 nm (e.g. Hamonou et al., 1999). We use level 2.0 (cloud screened and quality-assured) aerosol optical thickness (AOT) data in the following. The total uncertainty on AOT is <±0.01 for λ>440 nm and <±0.02 for λ<440 nm (Holben et al., 1998). Nevertheless, additional bias may exist when thin clouds are present and not screened in the AERONET level-2 products (Chew et al., 2011). To limit this, ground-based lidar profiles are used to identify the presence of clouds when sun photometer observations are available.

2.3 Airborne measurements

In this study, we also analyse extinction coefficients over the Atlantic, and in the vicinity of Henties Bay, acquired with the LNG Lidar (Bruneau et al., 2015) flown on the SAFIRE Falcon 20 on 5 and 6 September. The Falcon 20 operated from Walvis Bay, on the western coast of Namibia, roughly 100 km south of Henties Bay where the AEROCLO-sA supersite was located. Details on the Falcon payload as well as the on the flight plans conducted during these two days can be found in Formenti et al. (2019). In addition to the LNG data, we also make use of dynamical and thermodynamical data acquired offshore of Namibia with the Vaisala dropsonde system.

During the first flight (flight #6 in the morning of 5 September 2017), the Falcon operated from 0736 to 1014 UTC. It flew mostly above the continent to monitor dust emissions over the Etosha pan (see Formenti et al., 2019). The later portion of the flight was conducted over the sea (from 0930 to 1014 UTC), and a dropsonde was launched from 13.78°E/ 21.69°S at 0952 UTC. For the second flight (flight #9 in the morning of 6 September 2017), the Falcon 20 operated from 0703 to 0927 UTC and flew over the ocean from 0820 to 0927 UTC. Two dropsondes were launched from 11.92°E / 19.87°S at 0843 UTC and from 13.41°E / 22.23°S at 0908 UTC.

The LNG data over the sea are inversed using the same procedure as for the ground-based ALS lidar (see Appendix A) and utilizing the same lidar ratio vertical distribution (see values retrieved in Henties Bay for the two days in Section 3).

2.4 Spaceborne observations

2.4.1 CALIOP & CATS

The Cloud-Aerosol LIdar with Orthogonal Polarization (CALIOP) has been flying onboard the Cloud-Aerosol Lidar Pathfinder Satellite Observation (CALIPSO) since 2006 (https://www-calipso.larc.nasa.gov/products/). Details on the CALIOP instrument, data acquisition, and science products are given by Winker et al. (2007). In this work, we use CALIOP level-2 data, version 4.10, which was corrected for aerosol typing, as noted in Burton

https://doi.org/10.5194/acp-2019-507
Preprint. Discussion started: 3 June 2019

et al. (2012). The aerosol sorts identified in the free troposphere (FT) are typically polluted dust and elevated smoke (see example in Appendix A). These particles are likely composed of a majority of biomass burning aerosols originating from Angola and northeastern Namibia.

The CATS lidar orbited between 375 and 435 km onboard the non-sun-synchronous International Space Station (Yorks et al., 2016). It operated between January 2015 and October 2017 with the objective of measuring some cloud and aerosols properties which are useful for climate study. CATS flew over Namibia at various times during the AEROCLO-sA field campaign (Table 1). We mainly used the aerosol typing derived from CATS measurements, which is similar to the one established for CALIOP. The correspondence between the aerosol typing derived from CALIOP and CATS measurements are given in the Table 2. It should be noted that not all the aerosol types are named exactly in the same way. An example of aerosol typing is given in Appendix A.

Table 2: Lidar ratio (LR) corresponding with the CATS- and CALIOP-derived aerosol typing.

CALIOP/CATS Aerosol typing	Lidar ratio (sr) at 532 nm
Polluted continental or smoke/Polluted continental	70/65
Clean continental/Clean-background	53/55
Clean marine/Marine	23/25
Dust/Dust	44/45
Polluted dust/Dust mixture	55/35
Elevated smoke/Smoke	70/70
Dusty marine/Marine mixture	37/45

2.4.2 MODIS

The MODIS instruments (King et al., 1992; Salmonson et al., 1989) are aboard the Aqua and Terra platforms (http://modis-atmos.gsfc.nasa.gov). The polar orbit of Terra (http://terra.nasa.gov) passes over the equator from north to south in the morning, whereas Aqua (http://aqua.nasa.gov) has its ascending node over the equator during the afternoon. They provide a complete coverage of the Earth surface in one to two days with a resolution between 250 and 1000 m at ground level depending on the spectral band. We use the Terra and Aqua AOT at 550 nm from the MODIS aerosol product level-2 data. Both products are given with a spatial resolution of 10×10 km^2 at nadir. The standard deviation on the AOT retrieval (Remer et al., 2005) over land (ocean) is $0.15 \pm 0.05 AOT$ ($0.05 \pm 0.03 AOT$). The thermal anomalies derived from the MODIS fire product (e.g. Ichoku et al., 2008) are also used (https://modis.gsfc.nasa.gov/data/dataprod/mod14.php).

2.5 Modelling

The meteorological patterns are studied using Meteorological fields provided by the 6-hourly operational analyses of the European Centre for Medium-Range Weather Forecasts (ECMWF, http://apps.ecmwf.int/datasets/, Dee et al. (2011)). We also use the near real time analyses of atmospheric dynamics and aerosols from the Copernicus Atmosphere Monitoring Service (CAMS, https://atmosphere.copernicus.eu/). The calculations for synoptic

https://doi.org/10.5194/acp-2019-507
Preprint. Discussion started: 3 June 2019

Atmospheric Chemistry and Physics Discussions

analysis are computed on a 0.75-degree horizontal regular grid. Daily means are computed by averaging time steps at 03:00, 09:00, 15:00 and 21:00 UTC of daily forecasts initialised at 00.00 UTC. For local analyses, the meteorological wind fields are computed by using 1-h data on a 0.25-degree horizontal regular grid from the Fifth ECMWF Reanalysis (ERA5, https://www.ecmwf.int/en/forecasts/datasets/archive-datasets/reanalysis-datasets/era5, Hoffmann et al., 2018). The back trajectories analyses are based on the Hybrid Single Particle Lagrangian Integrated Trajectory (HYSPLIT) model (Draxler and Rolph, 2014; Stein et al., 2015). The wind fields used as input from the HYSPLIT model are from GDAS (Global Data Assimilation System, http://www.ncep.noaa.gov/) at 0.5° horizontal resolution. The isentropic ensemble mode with 24 individual back trajectories is computed to take into account the transport trajectory spread associated with the wind field. Using different modelling approaches allows the consistency of results to be verified.

3 Temporal evolution of the aerosol properties and vertical distribution over Henties Bay

The temporal evolution of the AOT at 550 nm derived from passive remote sensing observations (MODIS and the Henties Bay sun photometer) and 6-hourly CAMS fields between 22 August and 9 September 2017 are shown in Figure 2. For CAMS, both the AOT extracted from the grid cell centred on Henties Bay and the average AOT calculated on a 3x3 grid-point box surrounding the site are shown. There are little differences between the two CAMS-derived AOTs, which highlight the homogeneity of aerosol plumes overpassing Henties Bay according to the model and during that period. The MODIS AOT at 550 nm plotted in Figure 2 is a daily synthesis of Terra and Aqua products extracted over the sea only (see the black rectangle in Figure 1), to avoid mixing the effects of coast and surface albedo in the AOT retrievals. The ground-based lidar derived AOT at 355 nm (computed from the AEC) is not plotted in Figure 2 but given in Table 3. The AEC profiles shown in Figures 3 and 4 are obtained in cloud free conditions using a standard inversion procedure detailed in Appendix A. Most AEC profiles show clear air with low particle concentrations between the planetary boundary layer (PBL) and the elevated aerosol layer, with the notable exception of 2 September, when only aerosols are observed in the PBL (Figure 4b).

In Figure 2, three distinct periods can be identified based on the evolution of the CAMS-derived AOT at 550 nm. The optical and geometrical properties of the aerosol layers derived from the remote sensing instruments over Henties Bay during the 3 periods are summarized in Table 3. Integral optical properties are provided in both the PBL and the FT. The first period P_1 (22-28 August 2017, see lines highlighted in green in Table 3) is characterized by an averaged AOT of ~0.15 at 550 nm, while for the second period P_2 (28 August – 1 September 2017, see lines highlighted in orange in Table 3) the AOT increases to ~0.4. During the third period P_3 (3-9 September 2017), the average AOT is higher than during P_2 and around 0.55 at 550 nm. The variability of the CAMS-derived AOT is much larger during P_3 than during P_1 and P_2. The Angstrom exponent (AE) evolves during the period of interest, with AE~1 during P_1 et AE~1.4 during P_2 and P_3 (see Table 3), suggesting the presence of larger aerosol in the atmospheric column during P_1. However, the LR values associated with aerosols in the PBL and in the FT (23 and 55 sr, respectively) are the same for P_1 and P_2 (see Table 3) and suggest a predominance of clean marine aerosols in the PBL (Flamant et al., 1998) and the presence of terrigenous aerosols mixed with smoke. This is coherent with the polluted dust type inferred from the CALIOP observations in Figure A3a on 28 August 2017. Polluted dust corresponds to a mixture of dust and smoke aerosols in this region, with previously deposited dust from Etosha pan being remobilized by pyroconvection and mixed with BBA before being transported aloft. During P_2, MODIS highlights large AOT values (> 0.5 at 550 nm) over Angola and the Etosha pan (Figure 5a on 30 August 2017).

MODIS also evidences the existence of numerous fire hotspots (Figure 5b) over Angola, but also close to the Etosha pan area. The 650 hPa wind field also plotted in Figure 5a shows a high-pressure circulation over the area which favours the transport of dust and smoke aerosols in the FT towards the Henties Bay site. Furthermore, we observe a drastic change in terms of thickness of the elevated aerosol layer (~1.3 km during P_1 and ~2.5 km during P_2, Table 3) as well as in terms of maximum AEC in the FT (~0.12 km^{-1} during P_1 and ~0.25 km^{-1} during P_2, Table 3) as seen in the AEC profiles (compare Figure 3a-c for P_1 with Figure 3d-f and Figure 4a for P_2). The height of the base of the elevated aerosol layer also increases between the 2 periods, from 1.6 km to ~2.4 km (Table 3). These changes in optical and geometrical properties of the aerosols in the FT are related to the variability of long-range transport over the area, as discussed in Section 5.

Significant changes in aerosol optical properties are also observed between P_2 and P_3, with the LR values in the FT evolving from 55 to 70 sr and in the PBL from 23 to 55 sr, except on 8 and 9 September when LR values in the PBL are equal to 20 sr. During P_3, aerosols in the FT are identified as "smoke" (based on the CALIOP and CATS typing). Very few sun photometer data are available for LR retrieval due to the quasi permanent presence of a cloud cover over Henties Bay during the cycles of almucantar measurements. Nevertheless, such a measurement could be obtained during P_3, on 3 September 2017 at ~14:10 UTC. A sun photometer-derived LR value of ~63 sr at 532 nm was found to match the LR associated with the smoke type of CALIOP and CATS (i.e. 65-70 sr at 532 nm). The LR values observed in the PBL during P_3 (55 sr) between 3 and 7 September (Table 3) are higher than during P_2, which suggests the presence of a local mixture of terrigenous dust from coastal sources and anthropogenic pollution (Formenti et al., 2019). We observe a significant change in terms of thickness of the elevated aerosol layer (~2.5 km during P_2 and ~3.2 km during P_3, Table 3) as well as in terms of maximum AEC in the FT (~0.25 km^{-1} during P_2 and ~0.3 km^{-1} during P_3, Table 3), as seen in the AEC profiles (compare Figure 3d-f and Figure 4a for P_2 with Figure 4c-f for P_3). On the other hand, the height of the base of the elevated aerosol layer decreases between the 2 periods, from 2.4 km to ~1.75 km (Table 3).

Interestingly, during P_2 and P_3, the ground-based lidar measurements evidence the presence of layer of relatively high PDR (~10%) between the PBL (characterised by low PDR, i.e. <2%) and the elevated aerosol layers (~5%) as seen in Figure 3e-f and Figure 4a,c-f. The near-ground PDR values (<2%) indicate the presence of rather spherical particles. Above the PBL, the PDR values in excess of 5% indicate an aerosol mixing with the presence of large non-spherical particles, i.e. dust particles.

Overall, the AOTs from CAMS match perfectly the ones derived from both MODIS and the sun photometer, except on 2 September and 7-8 September. On 2 September a minimum in AOT is observed by the sun photometer which is not reproduced by CAMS simulations (even though a local minimum in the CAMS AOT can be seen). This may be explained by the coarse spatio-temporal sampling of the model, which is insufficient to highlight this sharp variation in AOT. Ground-based lidar AEC measurements on that day highlight the absence of aerosols in the FT (see Figure 4b). At the end of the measurement period (7 and 8 September), the sun photometer and MODIS are positively biased with respect to CAMS. This could be related to the presence of unscreened optically thin clouds such as the ones observed in the ground-based lidar data on 8 September (Figure A2d).

Table 3. Properties of aerosol layers above the Henties Bay site as derived from the ground-based lidar, CALIOP, CATS, the sun photometer and MODIS: lidar ratios for the free troposphere (LR_{FT}) and the planetary boundary layer LR_{PBL} at 532 nm, ground-based lidar (GBL)-derived AOT_{GBL} at 355 nm for the upper aerosol layer (UAL in bold) and the entire column as sampled by the lidar (Total), sun photometer-derived AOT_{phot} at 355 nm and 550 nm, sun photometer-derived Ångström exponent (AE), MODIS-derived AOT_{MODIS} in 0.5°x0.5° area over the sea close to Henties

https://doi.org/10.5194/acp-2019-507
Preprint. Discussion started: 3 June 2019

Atmospheric Chemistry and Physics Discussions
Open Access
EGU

Bay, UAL thickness and bottom height and maximum of the aerosol extinction coefficient (AEC_{max}) in the UAL. P_1 and P_2 correspond to periods when the UAL is mostly composed of "polluted dust", and P_3 corresponds to period when smoke aerosols dominate the composition of the UAL.

Date UTC	**LR_{FT}** LR_{PBL} (sr)	AOT_{GBL} at 355 nm **UAL** Total	AOT_{phot} at 355 nm *at 550 nm*	AE	AOT_{MODIS} 550 nm 0. 5°x0. 5°	UAL width (km)	UAL bottom height (km)	AEC_{max} in the UAL (km^{-1})
				Period P_1				
22/08 1400-1607	**55** 23	**0.17±0.01** 0.36±0.02	0.37±0.02 *0.22±0.01*	1.15±0.15	0.26±0.03	0.9	1.5	0.14
22/08 1608-2400	**55** 23	**0.17±0.04** 0.37±0.05	-	-	-	0.9	1.5	0.14
23/08 1645-2330	**55** 23	**0.16±0.01** 0.31±0.03	0.33±0.01 *0.22±0.01*	0.95±0.05	0.23±0.03	1.0	1.8	0.11
27/08 1545-1700	**55** 23	**0.22±0.01** 0.32±0.01	0.33 *0.18*	1.27	- (clouds)	2.5	1.6	0.09
				Period P_2				
28/08 1030-1230	**55** 23	**0.47±0.02** 0.63±0.03	0.59±0.04 *0.24±0.04*	1.5±0.05	0.25±0.12	3.0	1.7	0.21
29/08 1730-2250	**55** 23	**0.45±0.02** 0.60±0.03	-	-	- (clouds)	2.0	3.0	0.21
30/08 1800-2000	**55** 23	**0.55±0.05** 0.82±0.04	-	-	0.30±0.05	2.2	2.5	0.30
31/08 1430-1630	**55** 23	**0.66±0.03** 0.83±0.01	0.85±0.02 *0.42±0.08*	1.4±0.04	0.44±0.05	2.6	2.3	0.29
31/08 1631-2100	**55** 23	**0.51±0.08** 0.67±0.08	-	-	-	2.5	2.4	0.22
				Few aerosols in the FT				
02/09 0930-1130	**37** 18	**0.16±0.02** 0.32±0.02	0.28±0.03 *0.19±0.02*	0.9±0.1	- (clouds)	2.6	2.0	0.07
02/09 1715-1900	**37** 18	**0.04±0.01** 0.16±0.01	-	-	-	0.9	0.5	0.06
				Period P_3				
03/09 1400-1540	**70** 55	**0.85±0.08** 1.22±0.15	1.21±0.02 *0.65±0.01*	1.43±0.02	- (clouds)	4.8	1.2	0.23
04/09 2330-2400	**70** 55	**0.68±0.12** 0.81±0.15	-	-	- (clouds)	3.0	1.7	0.23
05/09 1400-1500	**70** 55	**0.82±0.12** 0.92±0.15	-	-	- (clouds)	2.3	2.2	0.33
06/09	**70**	**1.09±0.12**	1.34±0.06	1.50±0.04	0.56±0.11	3.0	3.0	0.41

https://doi.org/10.5194/acp-2019-507
Preprint. Discussion started: 3 June 2019

0830-1230	55	1.31±0.12	*0.70±0.05*					
07/09 1600-1904	**70** 55	**0.95±0.12** 1.28±0.16	1.30±0.04 *0.68±0.02*	1.46±0.01	0.74±0.03	3.0	2.7	0.32
08/09 1300-1500	**70** **20**	**0.59±0.03** 0.73±0.06	1.87 *1.01*	1.4	0.74±0.08	2.5	1.4	0.25
09/09 0900-1200	**70** 20	**0.84±0.11** 0.88±0.11	1.41±0.09 *0.75±0.01*	1.44±0.01	0.69±0.12	4.0	1.0	0.30

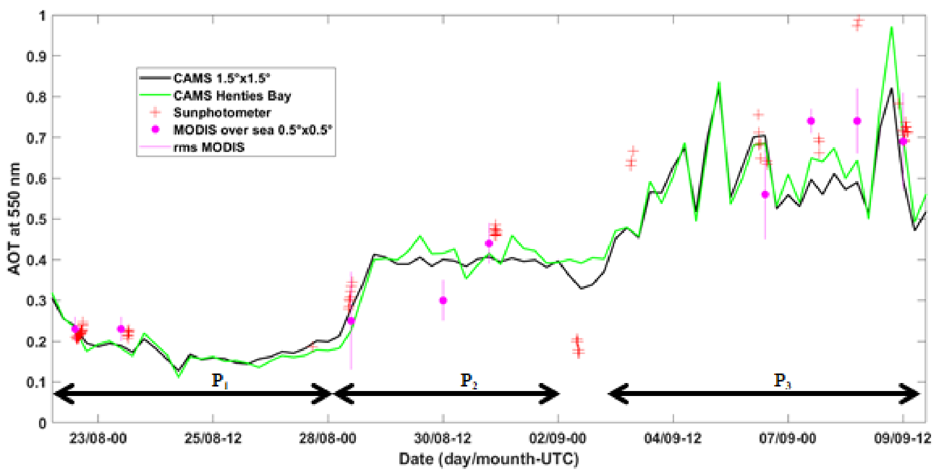

Figure 2: Temporal evolution of the AOT at 550 nm derived from CAMS (black and green solid lines), sun photometer (red crosses) and MODIS (magenta dots) data. The green solid line shows CAMS AOT extracted on the grid cell centred on Henties Bay. The black solid line shows the CAMS AOT averaged over 9 grid cells (a 3x3 grid box) centered on Henties Bay. The 3 periods highlighted by the AOT values (P_1, P_2 and P_3) are indicated.

https://doi.org/10.5194/acp-2019-507
Preprint. Discussion started: 3 June 2019

Atmospheric Chemistry and Physics Discussions

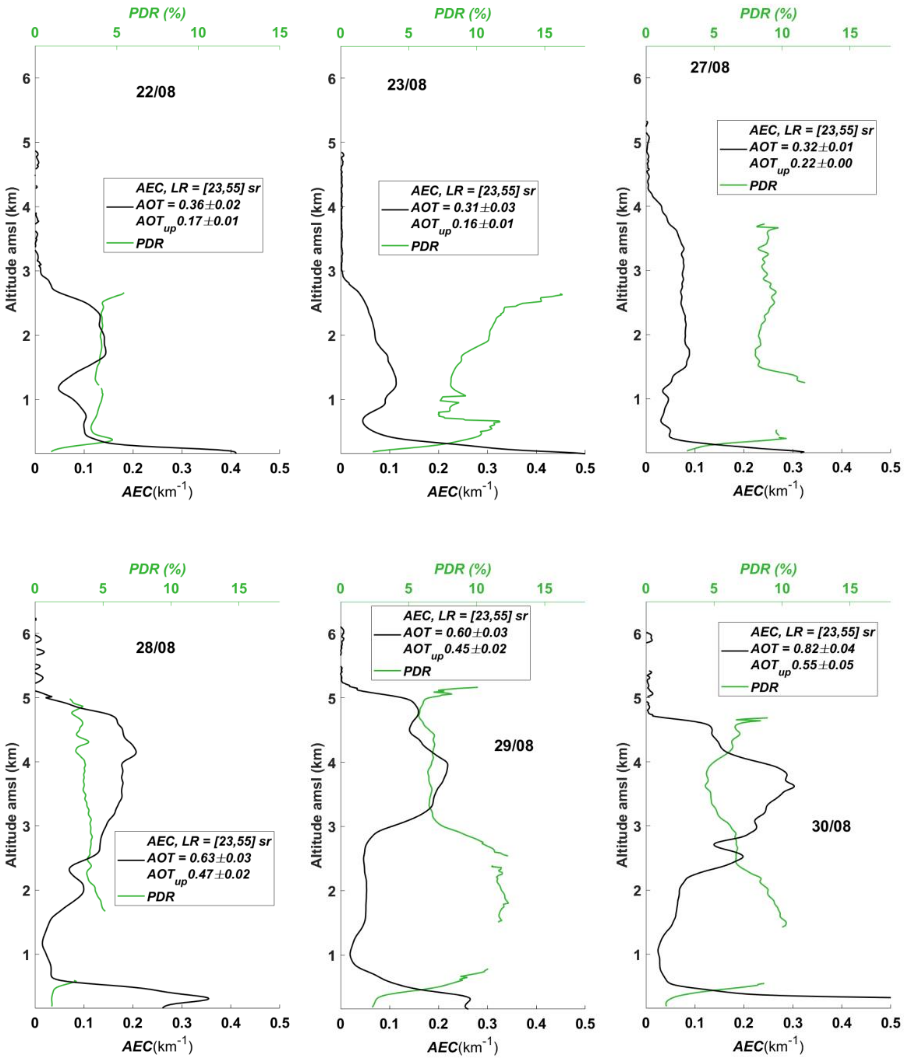

Figure 3: Vertical profiles of the aerosol extinction coefficient (AEC) and particle depolarization ratio (PDR) at 355 nm: on a) 22 (1400-1607 UTC), b) 23 (1645-2330 UTC), c) 27 (1545-1700 UTC), d) 28 (1030-1230 UTC), e) 29 (1730-2250 UTC) and f) 30 (1800-2000 UTC) August 2017. The total aerosol optical thickness (AOT) and the optical thickness of the upper aerosol layer (AOT_{up}) are also given.

https://doi.org/10.5194/acp-2019-507
Preprint. Discussion started: 3 June 2019

Atmospheric Chemistry and Physics Discussions

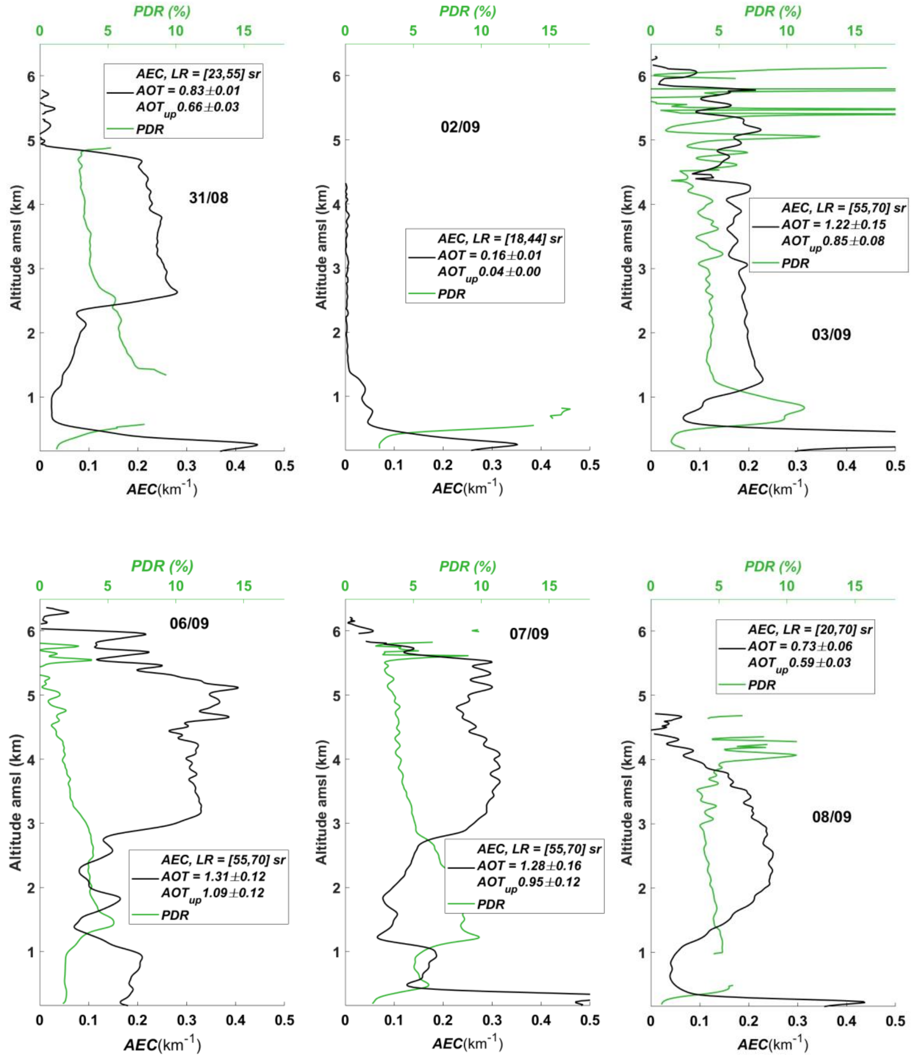

Figure 4: Vertical profiles of the aerosol extinction coefficient (AEC) and particle depolarization ratio (PDR) at 355 nm: on a) 31 (1430-1630 UTC) August, b) 2 (1715-1900 UTC), c) 3 (1400-1540 UTC), d) 6 (0830-1230 UTC), e) 7 (1600-1904 UTC) and f) 8 (1300-1500 UTC) September 2017. The total aerosol optical thickness (AOT) and the optical thickness of the upper aerosol layer (AOT$_{up}$) are also given.

https://doi.org/10.5194/acp-2019-507
Preprint. Discussion started: 3 June 2019

Atmospheric Chemistry and Physics
Discussions

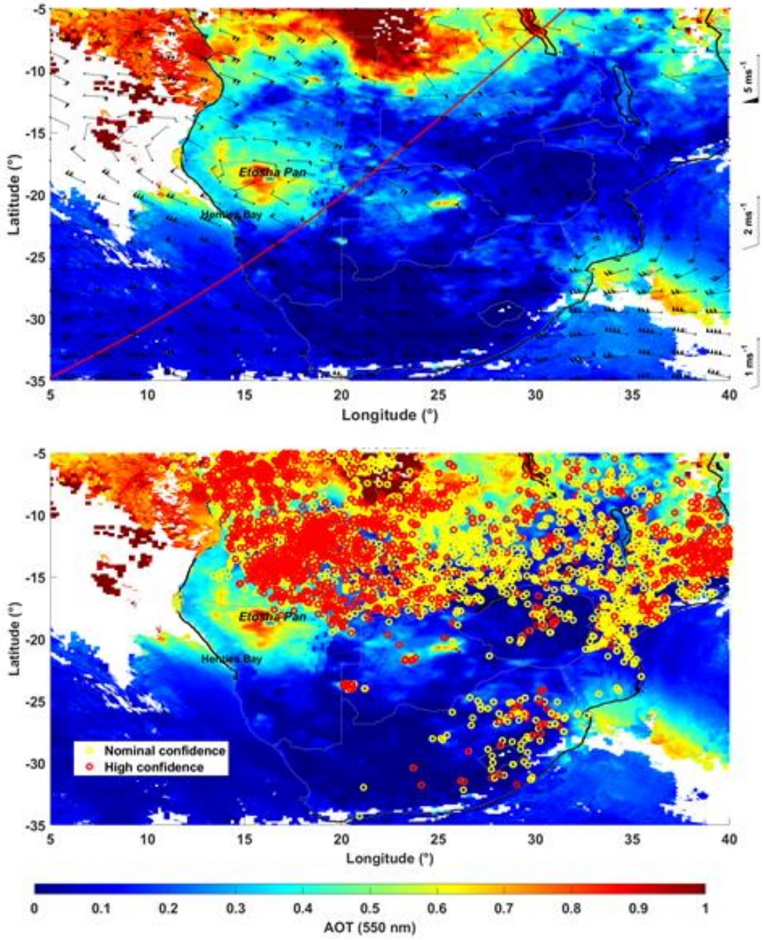

Figure 5: MODIS-derived (a) AOT and (b) fire hotspots on 30 August 2017. The ERA5 wind field at 650 hPa (~3.8 km AMSL) is also overlain. The night time ground track of CATS (b) is plotted with a red solid line (see Figure A3b).

4 Spatial variability of aerosol optical properties and vertical distribution from airborne observations

The purpose of this section is to highlight the spatial variability of the vertical structure of aerosols in the vicinity of Henties Bay through an analysis of the airborne lidar observations acquired offshore during two flights, on 5 and 6 September 2017. Airborne observations during AEROCLO-sA where only made during period P_3 (Formenti et al., 2019).

Figure 6a shows the three dimensional evolution of LNG-derived aerosol backscatter coefficient (ABC) profiles at 532 nm along the Falcon 20 flight track in the morning of 5 September 2017 following the methodology by Chazette and Totems (2017). LNG data highlight the presence of a widespread elevated BBA layer over the area of interest. The inversion of the LNG ABC data is performed using the same LRs as for the inversion of the ground-based lidar in Henties Bay (70 sr in the FT and 55 sr in the PBL, see Table 3). The average LNG-derived AEC profile shown in Figure 6b is obtained over the ocean between the two vertical dotted black lines in Figure 6a around 1000 UTC. Figure 7 shows the comparison between the dropsonde profiles of temperature, wind and relative humidity (RH) located over the ocean in Figure 6a and their counterparts extracted from ERA5 at 1000 UTC in a 0.25° x 0.25° grid centred on the Henties Bay site. There is a very good agreement between the vertical wind profiles (intensity and direction), nonetheless the wind is a little stronger on the dropsonde vertical profile, especially around 2 km AMSL, above the marine PBL, where it is in excess of 20 m s^{-1} (and less than 15 m s^{-1} in ERA5). The dropsonde measurements evidence the very sharp RH gradient at the top of the BBA layer (from 80% to nearly 1-2%, Figure 7b) at 6 km AMSL, this gradient being collocated with the large vertical gradient of AEC at 532 nm seen in the LNG data (Figure 6b). The high RH values in the elevated BBA layer are generally associated with the large amounts of water vapour released during wood combustion in wild fires (Haywood et al., 2003; Parmar et al., 2008). They also evidence a minimum of RH above the PBL, around 2 km AMSL, roughly coinciding with the base of the BBA layer (~2.2 km AMSL, Table 3). The sharp RH gradient at the top of the BBA layer is not well represented in the ERA5 analysis. The depth of the marine PBL is also seen to be thicker in the observations than in the model (Figure 7b), possibly because the ERA5 profiles is partly over the Namibian coast. The airborne lidar data evidence the presence of stratocumulus over the ocean around 1 km AMSL (Figure 6b, the absence of lidar data below that height indicating that the laser beam is completely extinguished in the cloud), close to the maximum of RH observed with the dropsonde (Figure 7b).

When comparing the mean vertical distribution of aerosols from the LNG-derived AEC profile offshore and the ground-based lidar AEC profile in Henties Bay averaged between 1400 and 1500 UTC (Figure 6b), we observe differences in terms of the altitude of the BBA layer top. Note that since the two lidars operate at different wavelengths, the AEC intensity is not directly comparable, but the vertical structure of AEC profiles is. On the other hand, we see that the bottom of the BBA layer is located at roughly the same altitude (Figure 6b). Furthermore, ERA5 analyses also evidence the fact that the dynamical and thermodynamical structure of the lower troposphere over Henties Bay did not evolve significantly between 1000 and 1500 UTC (not shown), except for an increase of RH between 5 and 6 km AMSL (by 20%, coherent with the apparition of clouds as seen in Figure A2c) and of wind speed at 4.5 km AMSL (by 5 m s^{-1}). Rather, the difference can be explained by regional scale circulation in the mid troposphere across the area. Over the ocean, ERA5 data indicates stronger northwest winds (~23 m s^{-1}) at the location of the airborne lidar AEC profile compared to the wind over Henties Bay (12 m s^{-1}) for the entire day on 5 September (not shown). The resulting horizontal wind shear between the Namibian coast and the ocean lead to differential advection within the BBA layer, and a different vertical structure of the aerosol layer between the coastline and over the ocean.

During the flight on 6 September 2017 (Figure 8a), LNG observations were made further offshore than on the previous day. In Figure 8b, we compare the AEC profiles acquired with LNG to the west and the northwest of Henties Bay (marked '1' and '2', respectively in Figure 8a) at ~0830 and ~0900 UTC, with the average AEC profile obtained between 0700 and 0930 UTC from the ground-based lidar in Henties Bay. Differences in the structure of the BBA layer appear between the offshore airborne lidar measurements from Henties Bay (profile '1' in Figure 8a) and the one further north (profile '2' in Figure 8a), the structure of the later being coherent with the ground-based AEC profile (Figure 8b). The structure of the elevated BBA layer observed from the AEC profiles in '1' and in Henties Bay match the structure of the RH and wind speed profiles from the southernmost dropsonde (Figure 9b), with a top (base) altitude of 5 km (3 km) AMSL. The wind in the BBA layer is observed to be rather

https://doi.org/10.5194/acp-2019-507
Preprint. Discussion started: 3 June 2019

Atmospheric Chemistry and Physics Discussions

constant and equal to 17 m s^{-1} on average as well as coming from the north. The maximum RH in the FT is ~55% and observed near the top of the BBA layer. Unlike what was observed the previous day, the RH above the top of the BBA layer is non negligible (~20%), which together with the AEC profile in Henties Bay, suggests the presence of a distinct aerosol layer above the main BBA layer, that is not seen in the AEC profile '1' (Figure 8b). The elevated BBA layer is separated from the PBL by a rather dry layer with small AECs, characterized by a strong wind shear (Figure 9b). The structure of the PBL observed in the AEC profile in Henties Bay mimics that seen in the RH profile, the PBL being capped by a moderate temperature inversion (3 K) but a significant RH gradient.

The AEC profile '2' derived from LNG observations and obtained ~100 km north of profile '1' exhibits a different structure than that of Henties Bay. The top of the BBA layer is observed to be slightly higher (5.2 km AMSL) while the altitude of the base of the BBA layer is the same (~3 km AMSL). The wind speed in the BBA layer as seen from the northernmost dropsonde (Figure 9a) is weaker than when it is closer to Henties Bay (Figure 8b), while the RH is higher throughout the lower troposphere, especially below the elevated BBA layer. The LNG profile in '2' exhibits significant AEC values below the base of the BBA layer observed further south, which may be partly related to the impact of RH on aerosol optical properties. The RH above the top of the BBA layer is non negligible (~20%), which together with the AEC profile in Henties Bay suggests the presence of a distinct aerosol layer above the main BBA layer, that is not seen in the AEC profile '1', but seen over Henties Bay (Figure 8b). A deep moist layer (including the PBL) is observed below the BBA layer.

In addition to the important variability in terms of vertical structure of the AEC profiles, it should be noted that the 550 nm AOT derived from the sun photometer in Henties Bay (0.70±0.05) is significantly higher than those determined from the airborne lidar data at 532 nm in '1' (0.37±0.06), but also significantly lower than that measured in '2' (1.13±0.10). Even though this may be partly related to the variability of RH and the hygroscopic growth of aerosols (e.g. Haslett et al., 2019), particularly below the BBA layer where RH is high in '2', the non-negligible AEC values between 5 and 6 km AMSL in Henties Bay (with AOT $\gtrsim$ 0.2 at 355 nm) and in '2' (with AOT $\gtrsim$ 0.08 at 532 nm) suggest that the aerosol may have a different origin than those below 5 km AMSL. Such a contribution was even more marked on the previous day (see Figure 6b), with an AOT at 532 nm above 5 km AMSL in excess of ~0.05.

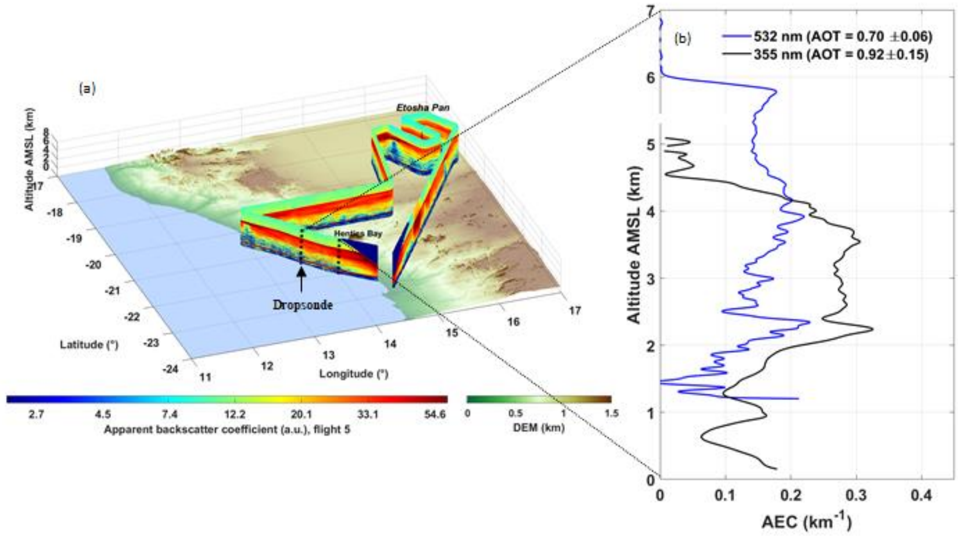

Figure 6: (a) Distance-height ("curtain-like") evolution of the LNG-derived apparent backscatter coefficient at 532 nm below the SAFIRE Falcon 20 during the morning flight on 5 September 2017. The location of the dropsonde released over the ocean is indicated as well as the location of the averaged LNG aerosol extinction coefficient (AEC) profile shown in (b) (between the 2 dotted vertical lines). (b) Vertical profiles of the AEC derived from the airborne lidar at 532 nm (~1000 UTC, blue solid line) and from the ground-based lidar at 355 nm (~1400-1500 UTC, black solid line).

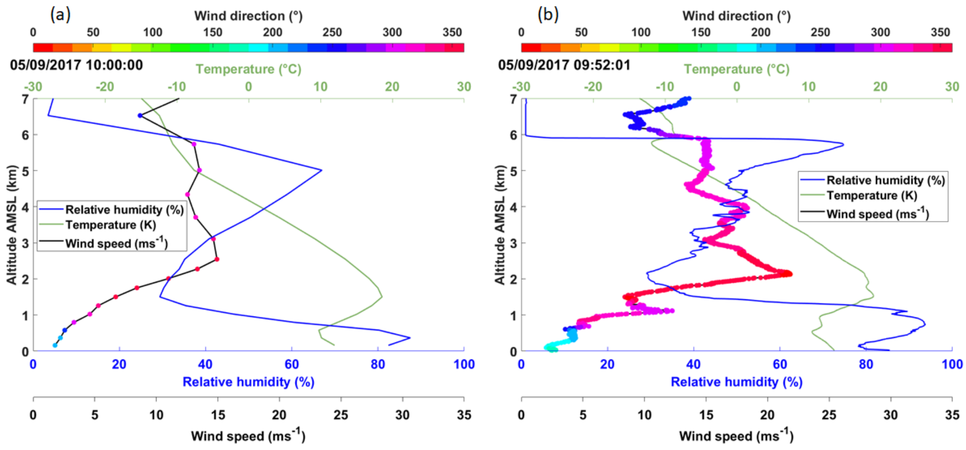

Figure 7: (a) Wind speed (black solid line), wind direction (coloured dots), RH (blue solid line) and temperature (green solid line) profiles extracted from ERA5 at 1000 UTC above Henties Bay over a 0.25° by 0.25° grid. (b) Same as (a) but measured by the dropsonde released over the ocean at 0952 UTC on 5 September 2017.

https://doi.org/10.5194/acp-2019-507
Preprint. Discussion started: 3 June 2019

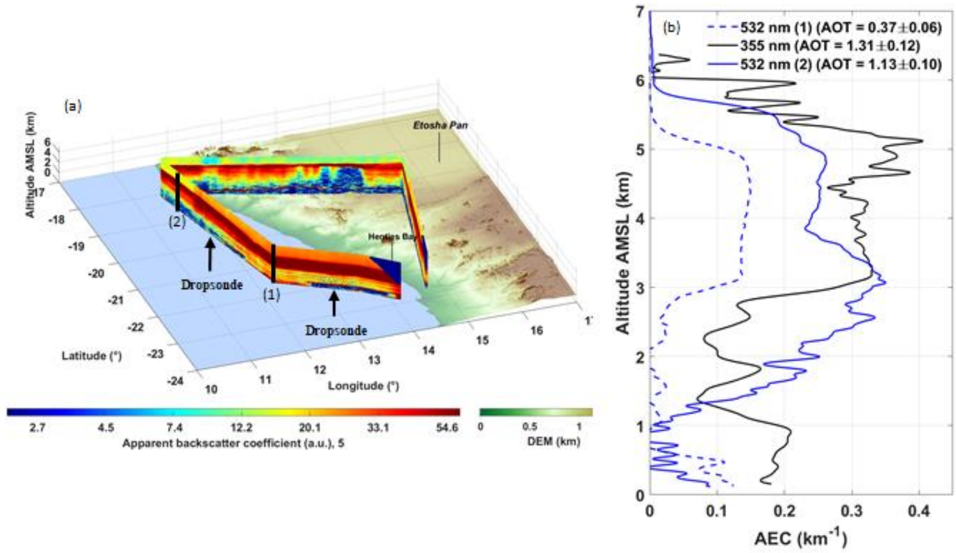

Figure 8: (a) Same as Figure 6a, but on 6 September 2017. The locations of the two launched dropsondes are also indicated by arrows. The lidar AEC profile labelled '1' shown in (b) is obtained after inversion of the LNG observations averaged between the two locations of the two dropsondes. The AEC profile labelled '2' is obtained after inversion of the lidar data between the northern most dropsonde and the northern end of the Falcon leg. (b) Vertical profiles of the AEC derived from the airborne lidar at 532 nm (~0830 and ~0900 UTC, for profile '2' (solid blue line) and '1' (dashed blue line), respectively) and from the ground-based lidar at 355 nm (~0700-0930 UTC, black solid line).

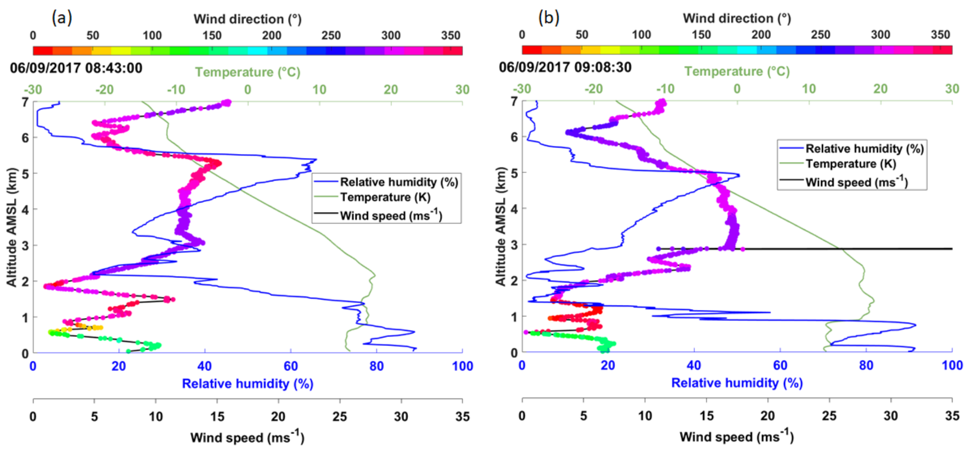

Figure 9: (a) & (b) Same as Figure 7b, but for the dropsondes released at 0843 UTC (to the northwest of Henties Bay) and at 0908 UTC (west of Henties Bay). The locations of the dropsondes are shown in Figure 8a.

5 Origin of elevated BBA layers over Henties Bay

Figure 10 shows the time-height evolution of hourly RH profiles from ERA5 between 22 August and 9 September 2017. The 3 periods (P_1, P_2 and P_3) identified from the AOT (Figure 2) are seen to correspond to distinct RH conditions in the mid troposphere, with rather dry conditions during P_1, then increased RH below 5 km AMSL

Atmospheric Chemistry and Physics Discussions

during P_2 and even more humid conditions below 6 km AMSL during P_3. For instance, the RH values between 2.5 and 5 km AMSL increases from values < 10% to values in excess of 60% between P_1 and P_2, which is most probably associated with the transport of BBA over Henties Bay. Likewise, the RH values between 5 and 6 km AMSL increases from 5% to ~70-80% between P_2 and P_3, which may be an indication of the transport of BBA from a different origin than during P_2. Periods P_2 and P_3 are clearly separated by an episode of very dry RH conditions on 2 September, the day also corresponding to a minimum of AOT over Henties Bay (Figure 2). In the following, we designed retro-trajectories analyses to investigate the origin of the 2 BBA layers in the FT seen in Figure 10.

A statistical study of the back trajectories of air masses ending over Henties Bay was designed to analyse the circulations related to the 3 identified periods P_1, P_2 and P_3. Six-day back-trajectories are initialized at 1200 UTC using the ensemble mode of the Lagrangian HYSPLIT model for which 27 trajectories are calculated for each selected altitude point over Henties Bay. Altitudes are discretised every 500 m between the base and the top of the BBA layers. The back trajectories are computed for days when ground-based lidar AEC profiles are available for Henties Bay (Table 3). A composite of the back trajectories is then made for the 3 different periods. Note that the heights selected for releasing the back trajectories are different for the 3 periods, namely between 1500 and 3000 m AMSL for P_1, between 3000 and 4500 m AMSL for P_2 and between 4000 and 6000 m AMSL for P_3, based on the information about the structure of the elevated aerosol layer in Table 3 and Figure 3 and 4. For each period, grey dots in Figure 10 represent the altitudes of the starting point of the uppermost and lowermost back trajectories for each of the days when lidar-derived AEC profiles are available. For periods P_2 and P_3, these altitudes are seen to be contained within atmospheric layers characterized by high RH values, corroborating the fact that BBA layers observed over Henties Bay are associated with high RHs.

For each period, more than 300 back trajectories are accumulated. To visualize the results, we used the two-dimensional histograms presented in Figure 11. The shapes of the two-dimensional histograms are clearly different between the 3 periods. During P_1, the density of trajectories is highest to the north of Henties Bay, and particularly along the Angola and Namibia coastline (Figure 11a). The air masses are turning counter clockwise before reaching Henties Bay, which is coherent with the presence of an upper level anticyclone over the continental plateau. The distribution of the trajectories suggests that the aerosols observed over Henties Bay mainly originate from Angola and northern Namibia (close to the back trajectories starting point) and are transported very rapidly towards the observational super site. There are a few trajectories coming from over the southern Atlantic Ocean. During P_2 (Figure 11b), the density of trajectories is highest along the Namibia coastline north of Henties Bay and over the ocean. The distribution of trajectories suggests that the BBA observed in Henties Bay originate from the continent (Angola) and have travelled a few hundred kilometres over the ocean before being transported back towards the southern African coastline. More trajectories are seen over the southern Atlantic Ocean than during P_1. There are also trajectories tracking back to Argentina. The density of back trajectories originating from South America increases significantly during P_3 (Figure 11c). They correspond to air masses arriving above 5000 m AMSL over Henties Bay. Two main transport pathways from South America to southern Africa are observed: a southern route where trajectories go as far south as 48°S before moving equatorward to Namibia and a more direct northern route where trajectories first follow the eastern coast of Brazil before heading due east towards Namibia. Transport from South America along the northern routes took 4 to 5 days to reach Henties Bay, whereas the transport along the southern route only took 2-3 days. The southern pathway is likely dominant, and the aerosols being transported

https://doi.org/10.5194/acp-2019-507
Preprint. Discussion started: 3 June 2019

are mainly associated with biomass burning occurring on 3-4 September 2017 over Brazil, Argentina and Paraguay, as shown from the MODIS-derived AOT fields and wild fire hotspots for that day (Figure 12a).
The aerosols released from the biomass burning over Amazonia are seen to be transported poleward over Argentina due to the strong winds at 500 hPa along the western flank of a high pressure centred over the eastern coast of Brazil (Figure 12b). A mid-tropospheric westerly jet then transports the aerosol plumes over the Atlantic Ocean (as seen also seen in Figure 12a) where they are then advected northward around the eastern edge of the high-pressure system over Brazil. The important cloud cover along the southern and eastern fringes of the high-pressure system does not allow the retrieval of AOTs with MODIS, except offshore of the Rio de la Plata estuary. The northward progression of the air masses transporting the BBA along the coast is further accelerated by the presence of a poleward moving cut-off low (centred at 40°S, 15°W) separating from the westerlies further south (Figure 12b). Over the following days, the cut-off low is seen to merge back with the westerlies while progressing eastward, and the high-pressure system at 500 hPa is observed to also move over the Atlantic Ocean and merge with the St Helena high on 5 September. On that day, the mid-tropospheric westerly jet already seen on 3 September (Figure 12b) transports the aerosols issued from wild fires over South America along the southern fringe of the St Helena high, which is centred at ~25°S and ~20°W. The westerly jet is associated with a dense mid-level cloud cover that prevents the retrieval of the AOT associated with the aerosols transported within the jet, except along its northern edge over Argentina and the western Atlantic Ocean, close to the coast of South America (Figure 12c). The jet is seen to extend quite far east over the Atlantic Ocean (from the combination of ERA5 winds and nebulosity) and to almost reach the southern tip of southern Africa. The aerosols travelling along the southern route with the westerly jet are then redirected towards Namibia by the strong northerly flow along the eastern flank of the St Helena high.
Closer to the Henties Bay, the occurrence of trajectories is highest along the northern Namibian coast, over the land. This suggests a more direct transport from the wild fire regions in Angola than during P_2 and even P_1. The occurrence of trajectories over the ocean just west of the southern African coast suggests that a significant part of the aerosols arriving in Henties Bay have travelled over the ocean before being transported back towards the continent, as already evidenced during P_2.

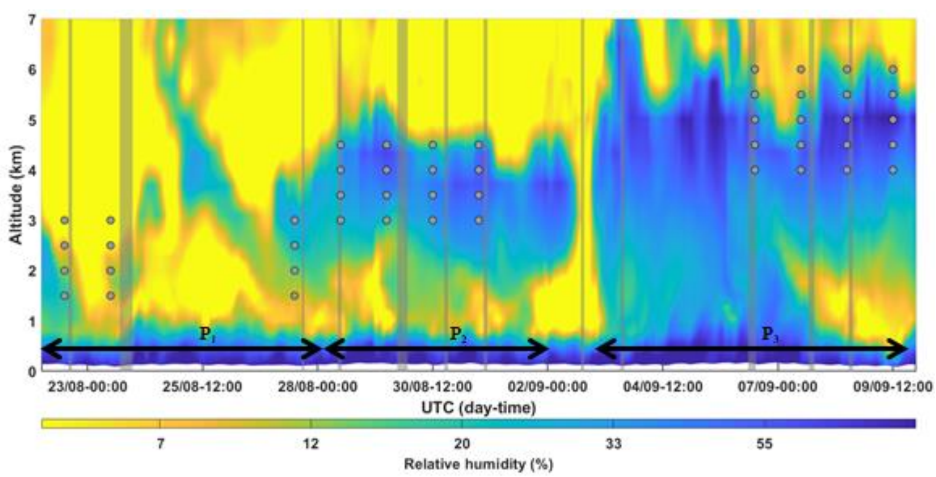

https://doi.org/10.5194/acp-2019-507
Preprint. Discussion started: 3 June 2019

Figure 10: Time-height evolution of the relative humidity vertical profiles derived from ERA5 above Henties Bay. The grey vertical lines indicate the time of the ground-based lidar profiles shown in Figure 3 and Figure 4. The thickness of the grey lines depends on the averaging period (the thicker the line, the longer the average). The 3 periods highlighted by the AOT values (P_1, P_2 and P_3) are also indicated. The grey dots represent the altitudes of the starting point of the uppermost and lowermost back trajectories for each of the days when lidar-derived AEC profiles are available.

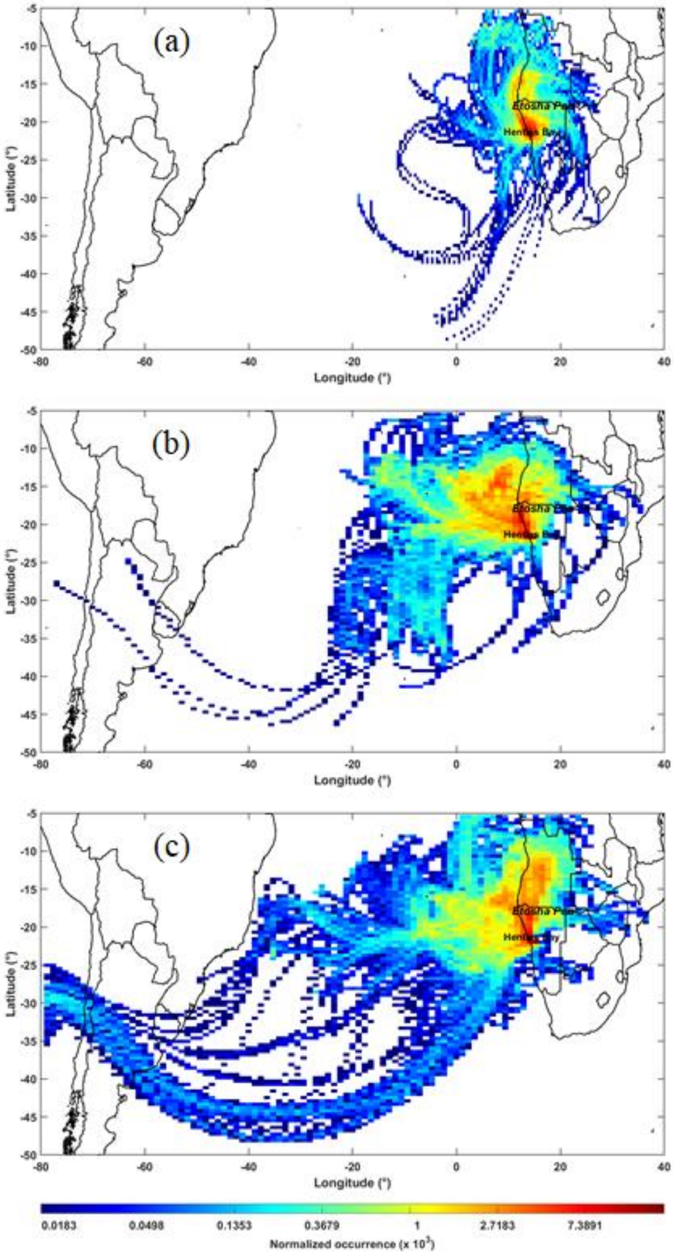

Figure 11: (a) Normalized occurrence of the back trajectories starting over Henties Bay at 1200 UTC on 22, 23 and 27 August 2017 between 1500 and 3000 m AMSL (period P_1). (b) Same as (a) but during P_2, for back trajectories from 28 to 31 August, between 3000 and 4500 m. (c) Same as (a) but during P_3, for trajectories from 6 to 9 September between

4000 and 6000 m. The calculations have been made using 6-day isentropic back trajectories with the HYSPLIT model (courtesy of NOAA Air Resources Laboratory; http://www.arl.noaa.gov) in ensemble mode.

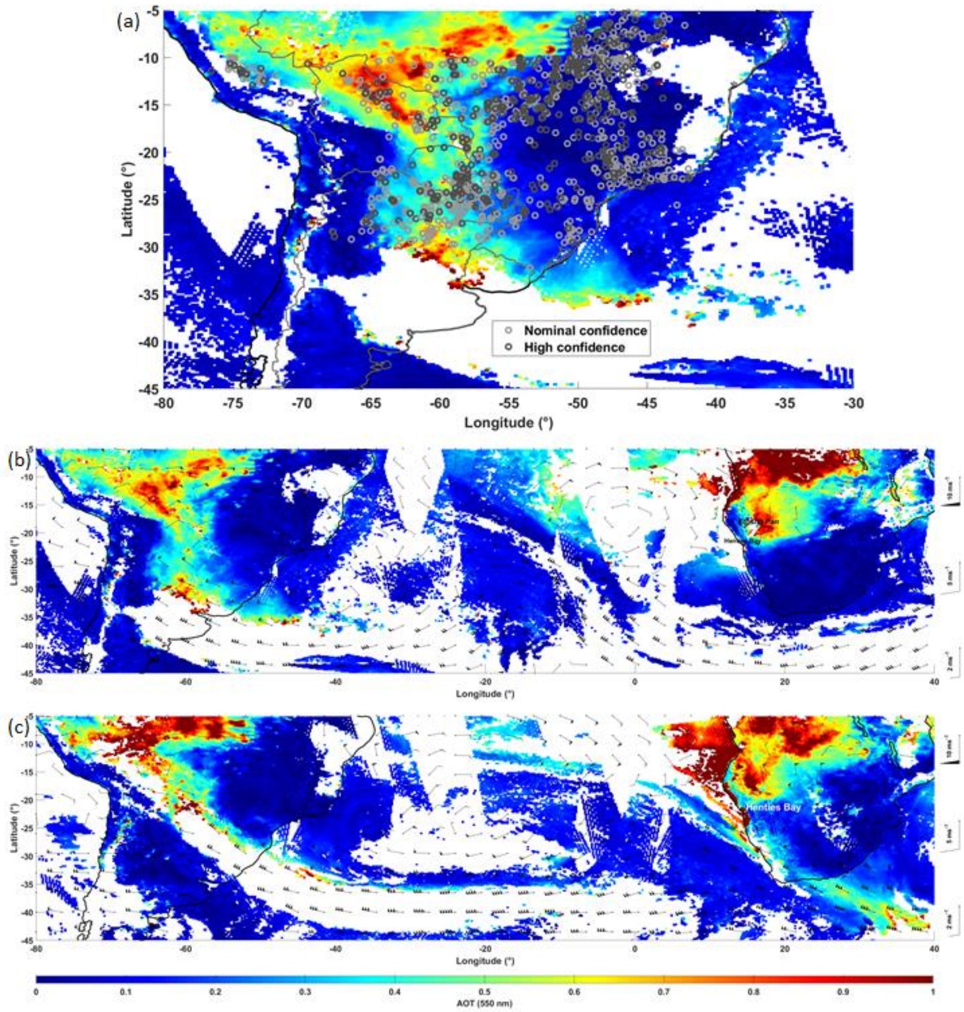

Figure 12: (a) MODIS-derived AOT at 550 nm and wild fire hotspots on 3 September 2017 over Brazil, Paraguay and Argentina. (b) MODIS-derived AOT and ERA5 wind field at 500 hPa on 3 September 2017. (c) Same as (b) but on 5 September 2017.

6 Conclusion

During the intensive field campaign of the AEROCLO-sA project (22 August - 12 September 2017), the very persistent cloud cover topping the marine boundary did not allow continuous ground-based monitoring of the aerosol layers above the stratocumulus deck, in the mid-troposphere. Nevertheless, the few available lidar observations that could be processed to retrieve AEC profiles allowed the first ever characterization of the aerosols layer advected over Henties Bay associated with different periods of transport (P_1, P_2 and P_3) from areas of biomass burning. The inversion of the ground-based lidar profiles was carried out using the constraints provided by the

https://doi.org/10.5194/acp-2019-507
Preprint. Discussion started: 3 June 2019

Atmospheric Chemistry and Physics Discussions

aerosol typing of the CALIOP and CATS space-borne instruments, but also the photometric measurements from AERONET network. The latter showed a good agreement with the MODIS AOT observations and the AOT outputs of the CAMS model. Differences were noted in the presence of high aerosol contents (AOT at 355 nm > 0.8) between the lidar- and sunphotometrer-derived AOTs, but those were likely due to the presence of clouds that were not detected by the passive sensors.

Using a combination of the above stated observations and back trajectory analyses, we evidence 3 periods with very different transport modes towards Henties Bay during the field campaign. The lowest AOTs (<0.2 at 550 nm) of the first period (P_1) are associated with air masses from Angola travelling along the Namibian and Angolan coasts. Intermediate AOTs (~0.4 at 550 nm) of the second period (P_2) are associated with polluted dusts (i.e. dust mixed with biomass burning aerosols from Angola), as well as dust from the Etosha Pan, which are recirculated above the ocean. During the third period (P_3), the largest AOTs (~0.7 at 550 nm) are observed. The atmospheric composition in the free troposphere for this period is the most remarkable. We highlight a significant contribution of forest fire aerosols from South America (Brazil, Argentina and Paraguay) with a plume transported to Henties Bay around 5000-6000 m AMSL (~10-15% of the low-middle troposphere AOT), i.e. above those coming from Angola that circulated over the Atlantic before reaching Henties Bay. The aerosol plume from South America is advected across the Atlantic Ocean along two main routes: one that follows the coast of Brazil before heading straight towards southern Africa, and one that follows the strong westerlies along the southern fringes of the St Helena high before heading north toward Namibia in connection with an equatorward moving cut-off low.

To the authors' knowledge, this is the first time that the evolution of the optical properties of aerosols trapped in the FT over coastal Namibia is evidenced, in link with the dominant transport patterns of lifted aerosols. It is also the first time that the contribution of the South American wild fires to the atmospheric composition over southern Africa is assessed on the basis of active and passive remote sensing observations and trajectory analyses. Highlighting the transport of BBA from South America and its advection on top of the BBA layers originating from Angola and northeast Namibia is of paramount importance in this region of the globe, where the feedback of aerosols and clouds on the radiative balance of the Earth system is still poorly known. The results presented here are therefore fundamental in order to provide realistic constraints to climate modelling by taking into better account of the origin, distribution against altitude and optical properties of biomass burning aerosols.

Furthermore, the temporal variability of BBA transport patterns from South America to southern Africa appears to be related to the variability of the Southern Annular Mode (SAM, i.e. the north-south movement of the westerly wind belt around Antarctica). Trenberth (2002) show that the SAM is the main driver of extratropical circulation in the Southern Hemisphere on weekly to decennial time scales, which is also the main driver of climate variability, affecting wildfire activity over South America (e.g. Holz et al., 2017). For instance, positive phases of the SAM (i.e. when a band of westerly winds contracts toward Antarctica) are associated primarily with warm conditions in the forested areas of South America, thereby favouring wild fire activity. On the other hand, negative phases lead to an expansion of the wind belt towards the lower latitudes, leading to the possibility for BBA transported in the westerlies to reach southern Africa in the austral winter. Given the possible short time scale of variability of the SAM, it is likely that the transport patterns to Henties Bay identified during period P_3 are related to a negative SAM phase, while during P_1 they are related to a positive phase. On longer time scales, climate modelling studies indicate a robust positive trend in the SAM for the end of this century (Lim et al., 2016), so that climate conditions conducive to an impact of the widespread South American fire activity in southern Africa will likely continue throughout the 21st century.

Acknowledgments. This work was supported by the French National Research Agency under grant agreement n° ANR-15-CE01-0014-01, the French national program LEFE/INSU, the Programme national de Télédetection Spatiale (PNTS, http://www.insu.cnrs.fr/pnts), grant n° PNTS-2016-14, the French National Agency for Space Studies (CNES), and the South African National Research Foundation (NRF) under grant UID 105958. The authors would also like to thank the AERIS data center for their support during the campaign and managing the AEROCLO-sA database. The research leading to these results has received funding from the European Union's 7th Framework Programme (FP7/2014-2018) under EUFAR2 contract n°312609". Airborne data was obtained using the aircraft managed by SAFIRE, the French facility for airborne research, an infrastructure of the French National Center for Scientific Research (CNRS), Météo-France and the French National Center for Space Studies (CNES). The authors would like to thank F. Blouzon and A. Abchiche (DT-INSU) as well as P. Genau and M. van Haecke (LATMOS) for their support in operating and processing the LNG data. The invaluable diplomatic assistance of the French Embassy in Namibia, the administrative support of the Service Partnership and Valorisation of the Regional Delegation of the Paris-Villejuif Region of the CNRS, and the cooperation of the Namibian National Commission on Research, Science and Technology (NCRST) are sincerely acknowledged. The long-term hosting and support of the SANUMARC, a research center of the University of Namibia in Henties Bay have been essential through the years and are warmly appreciated. The authors acknowledge the MODIS science, processing and data support teams for producing and providing MODIS data (at https://modis.gsfc.nasa.gov/data/dataprod/) and the NASA Langley Research Center Atmospheric Sciences Data Center for the data processing and distribution of CALIPSO products (level 4.10, at https://eosweb.larc.nasa.gov/HORDERBIN/HTML_Start.cgi). The authors would like to thank the AERONET network for sun photometer products (at https://aeronet.gsfc.nasa.gov/).

Data availability. The aircraft and ground-based data used here can be accessed using the AEROCLO-sA database at http://baobab.sedoo.fr/AEROCLO-sA/. An embargo period of 2 years after the upload applies. After that, external users can access the data in the same way as AEROCLO-sA participants before that time. Before the end of the embargo period, external users can request the release of individual datasets. It is planned for AEROCLO-sA data to get DOIs, but this has not been carried out for all datasets yet. The back trajectories data can be obtained upon request to the first author of the paper.

Author contributions. PC inverted the ground-based and airborne lidar data, analyzed the data and wrote the paper; CF analyzed the data and wrote the paper; JT assembled and calibrated the ground-based lidar, MG participated to the study of atmospheric dynamic and to the paper editing, GS participated to the back-trajectories computation, AB gathered the CATS lidar data and the wind fields, PF coordinated the AEROCLO-sA project, XL participated in the pre- and post-field calibration and operation of the lidar, KD and JFD maintained and operated the lidar during the field campaign.

Competing interests. The authors declare that they have no conflict of interest.

https://doi.org/10.5194/acp-2019-507
Preprint. Discussion started: 3 June 2019

Special issue statement. This article is part of the special issue "New observations and related modeling studies of the aerosol–cloud–climate system in the Southeast Atlantic and southern Africa regions" (ACP/AMT inter-journal SI)". It is not associated with a conference.

7 References

Ackerman, A. S., Toon, O. B., Stevens, D. E., Heymsfield, A. J., Ramanathan, V. and Welton, E. J.: Reduction of tropical cloudiness by soot, Science, 288(5468), 1042–7, doi:10.1126/SCIENCE.288.5468.1042, 2000.

Adebiyi, A. A. and Zuidema, P.: The role of the southern African easterly jet in modifying the southeast Atlantic aerosol and cloud environments, Q. J. R. Meteorol. Soc., 142(697), 1574–1589, doi:10.1002/qj.2765, 2016.

Adebiyi, A. A., Zuidema, P. and Abel, S. J.: The convolution of dynamics and moisture with the presence of shortwave absorbing aerosols over the southeast Atlantic, J. Clim., 28(5), 1997–2024, doi:10.1175/JCLI-D-14-00352.1, 2015.

Andreae, M. O., Elbert, W. and de Mora, S. J.: Biogenic sulfur emissions and aerosols over the tropical South Atlantic: 3. Atmospheric dimethylsulfide, aerosols and cloud condensation nuclei, J. Geophys. Res., 100(D6), 11335, doi:10.1029/94jd02828, 2004.

Ångström, A.: The parameters of atmospheric turbidity, Tellus A, 16, 64–75, doi:10.3402/tellusa.v16i1.8885, 1964.

Bates, T. S., Quinn, P. K., Coffman, D. J., Johnson, J. E., Miller, T. L., Covert, D. S., Wiedensohler, A., Leinert, S., Nowak, A. and Neusüss, C.: Regional physical and chemical properties of the marine boundary layer aerosol across the Atlantic during Aerosols99: An overview, J. Geophys. Res. Atmos., 106(D18), 20767–20782, doi:10.1029/2000JD900578, 2001.

Burton, S. P., Ferrare, R. A., Hostetler, C. A., Hair, J. W., Rogers, R. R., Obland, M. D., Butler, C. F., Cook, A. L., Harper, D. B. and Froyd, K. D.: Aerosol classification using airborne High Spectral Resolution Lidar measurements – methodology and examples, Atmos. Meas. Tech., 5(1), 73–98, doi:10.5194/amt-5-73-2012, 2012.

Chazette, P.: The monsoon aerosol extinction properties at Goa during INDOEX as measured with lidar, J. Geophys. Res., 108(D6), 4187, doi:10.1029/2002JD002074, 2003.

Chazette, P. and Totems, J.: Mini N2-Raman Lidar onboard ultra-light aircraft for aerosol measurements: Demonstration and extrapolation, Remote Sens., 9(12), doi:10.3390/rs9121226, 2017.

Chazette, P., Bocquet, M., Royer, P., Winiarek, V., Raut, J. C., Labazuy, P., Gouhier, M., Lardier, M. and Cariou, J. P.: Eyjafjallajökull ash concentrations derived from both lidar and modeling, J. Geophys. Res. Atmos., 117, doi:10.1029/2011JD015755, 2012a.

Chazette, P., Dabas, a., Sanak, J., Lardier, M. and Royer, P.: French airborne lidar measurements for Eyjafjallajökull ash plume survey, Atmos. Chem. Phys., 12(15), 7059–7072, doi:10.5194/acp-12-7059-2012, 2012b.

Chew, B. N., Campbell, J. R., Reid, J. S., Giles, D. M., Welton, E. J., Salinas, S. V. and Liew, S. C.: Tropical cirrus cloud contamination in sun photometer data, Atmos. Environ., 45(37), 6724–6731, doi:10.1016/j.atmosenv.2011.08.017, 2011.

Costantino, L. and Bréon, F.-M.: Aerosol indirect effect on warm clouds over South-East Atlantic, from co-located MODIS and CALIPSO observations, Atmos. Chem. Phys., 13(1), 69–88, doi:10.5194/acp-13-69-2013, 2013.

Costantino, L. and Bréon, F. M.: Analysis of aerosol-cloud interaction from multi-sensor satellite observations, Geophys. Res. Lett., 37(11), doi:10.1029/2009GL041828, 2010.

Dee, D. P., Uppala, S. M., Simmons, A. J., Berrisford, P., Poli, P., Kobayashi, S., Andrae, U., Balmaseda, M. A., Balsamo, G., Bauer, P., Bechtold, P., Beljaars, A. C. M., van de Berg, L., Bidlot, J., Bormann, N., Delsol, C., Dragani, R., Fuentes, M., Geer, A. J., Haimberger, L., Healy, S. B., Hersbach, H., Hólm, E. V, Isaksen, L., Kållberg, P., Köhler, M., Matricardi, M., Mcnally, A. P., Monge-Sanz, B. M., Morcrette, J. J., Park, B. K., Peubey, C., de Rosnay, P., Tavolato, C., Thépaut, J. N. and Vitart, F.: The ERA-Interim reanalysis: Configuration and performance of the data assimilation system, Q. J. R. Meteorol. Soc., 137(656), 553–597, 2011.

Dieudonné, E., Chazette, P., Marnas, F., Totems, J. and Shang, X.: Raman Lidar Observations of Aerosol Optical Properties in 11 Cities from France to Siberia, Remote Sens., 9(10), 978, doi:10.3390/rs9100978, 2017.

Draxler, R. R. R. and Rolph, G. D. D.: HYSPLIT (HYbrid Single-Particle Lagrangian Integrated Trajectory) Model access via NOAA ARL READY Website (http://www.arl.noaa.gov/HYSPLIT.php). NOAA Air Resources Laboratory, College Park, MD., NOAA Air Resour. Lab. [online] Available from: http://ready.arl.noaa.gov/HYSPLIT_ash.php, 2014.

Formenti, P., D'Anna, B., Flamant, C., Mallet, M. D., Piketh, S. J., Schepanski, K., Waquet, F., Auriol, F., Brogniez, G., Burnet, F., Chaboureau, J.-P., Chauvigné, A., Chazette, P., Denjean, C., Desboeufs, K., Doussin, J.-F., Elguindi, N., Feuerstein, S., Gaetani, M., Giorio, C., Klopper, D., Mallet, M. D., Nabat, P., Monod, A., Solmon, F., Namwoonde, A., Chikwililwa, C., Mushi, R., Welton, E. J., Holben, B., Formenti, P., D'Anna, B., Flamant, C., Mallet, M. D., Piketh, S. J., Schepanski, K., Waquet, F., Auriol, F., Brogniez, G., Burnet, F., Chaboureau, J.-P., Chauvigné, A., Chazette, P., Denjean, C., Desboeufs, K., Doussin, J.-F., Elguindi, N., Feuerstein, S., Gaetani, M., Giorio, C., Klopper, D., Mallet, M. D., Nabat, P., Monod, A., Solmon, F., Namwoonde, A., Chikwililwa, C., Mushi, R., Welton, E. J. and Holben, B.: The Aerosols, Radiation and Clouds in southern Africa (AEROCLO-sA) field campaign in Namibia: overview, illustrative observations and way forward, Bull. Am. Meteorol. Soc., BAMS-D-17-0278.1, doi:10.1175/BAMS-D-17-0278.1, 2019.

Fuchs, J., Cermak, J., Andersen, H., Hollmann, R. and Schwarz, K.: On the Influence of Air Mass Origin on Low-Cloud Properties in the Southeast Atlantic, J. Geophys. Res. Atmos., 122(20), 11,076-11,091, doi:10.1002/2017JD027184, 2017.

Ginoux, P., Prospero, J. M., Gill, T. E., Hsu, N. C. and Zhao, M.: Global-scale attribution of anthropogenic and natural dust sources and their emission rates based on MODIS Deep Blue aerosol products, Rev. Geophys., 50(3), 1–36, doi:10.1029/2012RG000388, 2012.

Gordon, H., Field, P. R., Abel, S. J., Dalvi, M., Grosvenor, D. P., Hill, A. A., Johnson, B. T., Miltenberger, A. K., Yoshioka, M. and Carslaw, K. S.: Large simulated radiative effects of smoke in the south-east Atlantic, Atmos. Chem. Phys., 18(20), 15261–15289, doi:10.5194/acp-18-15261-2018, 2018.

Hamonou, E., Chazette, P., Balis, D., Dulac, F., Schneider, X., Galani, E., Ancellet, G. and Papayannis, A.: Characterization of the vertical structure of Saharan dust export to the Mediterranean basin, J. Geophys. Res., 104(D18), 22257, doi:10.1029/1999JD900257, 1999.

Haslett, S. L., Taylor, J. W., Deetz, K., Vogel, B., Babić, K., Kalthoff, N., Wieser, A., Dione, C., Lohou, F., Brito, J., Dupuy, R., Schwarzenboeck, A., Zieger, P. and Coe, H.: The radiative impact of out-of-cloud aerosol hygroscopic growth during the summer monsoon in southern West Africa, Atmos. Chem. Phys., 19(3), 1505–1520, doi:10.5194/acp-19-1505-2019, 2019.

Haywood, J. M., Osborne, S. R., Francis, P. N., Keil, A., Formenti, P., Andreae, M. O. and Kaye, P. H.: The mean physical and optical properties of regional haze dominated by biomass burning aerosol measured from the C-130 aircraft during SAFARI 2000, J. Geophys. Res. Atmos., 108(D13), n/a-n/a, doi:10.1029/2002jd002226, 2003.

Hoffmann, L., Günther, G., Li, D., Stein, O., Wu, X., Griessbach, S., Heng, Y., Konopka, P., Müller, R., Vogel, B. and Wright, J. S.: From ERA-Interim to ERA5: considerable impact of ECMWF's next-generation reanalysis on Lagrangian transport simulations, Atmos. Chem. Phys. Discuss., 1–38, doi:10.5194/acp-2018-1199, 2018.

Holben, B. N., Eck, T. F., Slutsker, I., Tanré, D., Buis, J. P., Setzer, A., Vermote, E., Reagan, J. A., Kaufman, Y. J., Nakajima, T., Lavenu, F., Jankowiak, I. and Smirnov, A.: AERONET—A Federated Instrument Network and Data Archive for Aerosol Characterization, Remote Sens. Environ., 66(1), 1–16, doi:10.1016/S0034-4257(98)00031-5, 1998.

Holz, A., Paritsis, J., Mundo, I. A., Veblen, T. T., Kitzberger, T., Williamson, G. J., Aráoz, E., Bustos-Schindler, C., González, M. E., Grau, H. R. and Quezada, J. M.: Southern Annular Mode drives multicentury wildfire activity in southern South America., Proc. Natl. Acad. Sci. U. S. A., 114(36), 9552–9557, doi:10.1073/pnas.1705168114, 2017.

Ichoku, C., Giglio, L., Wooster, M. J. and Remer, L. A.: Global characterization of biomass-burning patterns using satellite measurements of fire radiative energy, Remote Sens. Environ., 112(6), 2950–2962, doi:10.1016/j.rse.2008.02.009, 2008.

Johansson, L., Jalkanen, J. P. and Kukkonen, J.: Global assessment of shipping emissions in 2015 on a high spatial and temporal resolution, Atmos. Environ., 167, 403–415, doi:10.1016/j.atmosenv.2017.08.042, 2017.

Jones, A. and Haywood, J. M.: Sea-spray geoengineering in the HadGEM2-ES earth-system model: radiative impact and climate response, Atmos. Chem. Phys., 12(22), 10887–10898, doi:10.5194/acp-12-10887-2012, 2012.

Jones, A., Haywood, J. and Boucher, O.: Climate impacts of geoengineering marine stratocumulus clouds, J. Geophys. Res. Atmos., 114(10), D10106, doi:10.1029/2008JD011450, 2009.

Keil, A. and Haywood, J. M.: Solar radiative forcing by biomass burning aerosol particles during SAFARI 2000: A case study based on measured aerosol and cloud properties, J. Geophys. Res. Atmos., 108(D13), n/a-n/a, doi:10.1029/2002jd002315, 2003.

King, M. D., Kaufman, Y. J., Menzel, W. P. and Tanré, D.: Remote Sensing of Cloud, Aerosol, and Water Vapor Properties from the Moderate Resolution Imaging Spectrometer (MODIS), IEEE Trans. Geosci. Remote Sens., 30(1), 2–27, doi:10.1109/36.124212, 1992.

Léon, J.-F., Chazette, P., Pelon, J., Dulac, F., Randriamiarisoa, H., patrick Chazette, Pelon, J., Dulac, F. and Randriamiarisoa, H.: Aerosol direct radiative impact over the INDOEX area based on passive and active remote sensing, J. Geophys. Res., 107(D19), 8006, doi:10.1029/2000JD000116, 2002.

Lim, E.-P., Hendon, H. H., Arblaster, J. M., Delage, F., Nguyen, H., Min, S.-K. and Wheeler, M. C.: The impact

https://doi.org/10.5194/acp-2019-507
Preprint. Discussion started: 3 June 2019

Atmospheric Chemistry and Physics Discussions

of the Southern Annular Mode on future changes in Southern Hemisphere rainfall, Geophys. Res. Lett., 43(13), 7160–7167, doi:10.1002/2016GL069453, 2016.

McFarquhar, G. M. and Wang, H.: Effects of aerosols on trade wind cumuli over the Indian Ocean: Model simulations, Q. J. R. Meteorol. Soc., 132(616), 821–843, doi:10.1256/qj.04.179, 2006.

Müller, D., Ansmann, A., Mattis, I., Tesche, M., Wandinger, U., Althausen, D. and Pisani, G.: Aerosol-type-dependent lidar ratios observed with Raman lidar, J. Geophys. Res., 112(D16), D16202, doi:10.1029/2006JD008292, 2007.

Myhre, G., Samset, B. H., Schulz, M., Balkanski, Y., Bauer, S., Berntsen, T. K., Bian, H., Bellouin, N., Chin, M., Diehl, T., Easter, R. C., Feichter, J., Ghan, S. J., Hauglustaine, D., Iversen, T., Kinne, S., Kirkevåg, A., Lamarque, J.-F., Lin, G., Liu, X., Lund, M. T., Luo, G., Ma, X., van Noije, T., Penner, J. E., Rasch, P. J., Ruiz, A., Seland, Ø., Skeie, R. B., Stier, P., Takemura, T., Tsigaridis, K., Wang, P., Wang, Z., Xu, L., Yu, H., Yu, F., Yoon, J.-H., Zhang, K., Zhang, H. and Zhou, C.: Radiative forcing of the direct aerosol effect from AeroCom Phase II simulations, Atmos. Chem. Phys., 13(4), 1853–1877, doi:10.5194/acp-13-1853-2013, 2013.

Nicolet, M.: On the molecular scattering in the terrestrial atmosphere : An empirical formula for its calculation in the homosphere, Planet. Space Sci., 32(11), 1467–1468, doi:10.1016/0032-0633(84)90089-8, 1984.

Parmar, R. S., Welling, M., Andreae, M. O. and Helas, G.: Water vapor release from biomass combustion, Atmos. Chem. Phys., 8(20), 6147–6153, doi:10.5194/acp-8-6147-2008, 2008.

Ramanathan, V., Li, F., Ramana, M. V, Praveen, P. S., Kim, D., Corrigan, C. E., Nguyen, H., Stone, E. A., Schauer, J. J., Carmichael, G. R., Adhikary, B. and Yoon, S. C.: Atmospheric brown clouds: Hemispherical and regional variations in long-range transport, absorption, and radiative forcing, J. Geophys. Res, 112, 22–21, doi:10.1029/2006JD008124, 2007.

Raut, J.-C. and Chazette, P.: Radiative budget in the presence of multi-layered aerosol structures in the framework of AMMA SOP-0, Atmos. Chem. Phys., 8(4), 12461–12528, doi:10.5194/acpd-8-12461-2008, 2008.

Raut, J.-C. and Chazette, P.: Assessment of vertically-resolved PM<inf>10</inf> from mobile lidar observations, Atmos. Chem. Phys., 9(21), 2009.

Remer, L. A., Kaufman, Y. J., Tanré, D., Mattoo, S., Chu, D. A., Martins, J. V., Li, R.-R., Ichoku, C., Levy, R. C., Kleidman, R. G., Eck, T. F., Vermote, E. and Holben, B. N.: The MODIS Aerosol Algorithm, Products, and Validation, J. Atmos. Sci., 62(4), 947–973, doi:10.1175/JAS3385.1, 2005.

Royer, P., Chazette, P., Lardier, M. and Sauvage, L.: Aerosol content survey by mini N<inf>2</inf>-Raman lidar: Application to local and long-range transport aerosols, Atmos. Environ., 45(39), doi:10.1016/j.atmosenv.2010.11.001, 2011a.

Royer, P., Chazette, P., Lardier, M. and Sauvage, L.: Aerosol content survey by mini N2-Raman lidar: Application to local and long-range transport aerosols, Atmos. Environ., 45(39), 7487–7495, doi:10.1016/j.atmosenv.2010.11.001, 2011b.

Royer, P., Chazette, P., Sartelet, K., Zhang, Q. J., Beekmann, M. and Raut, J.-C.: Comparison of lidar-derived PM_{10} with regional modeling and ground-based observations in the frame of MEGAPOLI experiment, Atmos. Chem. Phys., 11(20), 10705–10726, doi:10.5194/acp-11-10705-2011, 2011c.

Salmonson, V. V., Barnes, W. L. L., Maymon, P. W. P. W. P. W., Montgomery, H. E. H. E. and Ostrow, H.: MODIS: Advanced Facility Instrument for Studies of the Earth as a System, IEEE Trans. Geosci. Remote Sens., 27(2), 145–153, doi:10.1109/36.20292, 1989.

Stein, A. F., Draxler, R. R., Rolph, G. D., Stunder, B. J. B., Cohen, M. D., Ngan, F., Stein, A. F., Draxler, R. R., Rolph, G. D., Stunder, B. J. B., Cohen, M. D. and Ngan, F.: NOAA's HYSPLIT Atmospheric Transport and Dispersion Modeling System, Bull. Am. Meteorol. Soc., 96(12), 2059–2077, doi:10.1175/BAMS-D-14-00110.1, 2015.

Stier, P., Schutgens, N. A. J., Bellouin, N., Bian, H., Boucher, O., Chin, M., Ghan, S., Huneeus, N., Kinne, S., Lin, G., Ma, X., Myhre, G., Penner, J. E., Randles, C. A., Samset, B., Schulz, M., Takemura, T., Yu, F., Yu, H. and Zhou, C.: Host model uncertainties in aerosol radiative forcing estimates: results from the AeroCom Prescribed intercomparison study, Atmos. Chem. Phys., 13(6), 3245–3270, doi:10.5194/acp-13-3245-2013, 2013.

Trenberth, K. E.: Interannual Variability of the 500 mb Zonal Mean Flow in the Southern Hemisphere, Mon. Weather Rev., 107(11), 1515–1524, doi:10.1175/1520-0493(1979)107<1515:ivotmz>2.0.co;2, 2002.

Tyson, P. D. and Preston-White, R. A.: The weather and climate of southern Africa, Oxford University Press. [online] Available from: https://global.oup.com/academic/product/the-weather-and-climate-of-southern-africa-9780195718065?lang=en&cc=in (Accessed 29 April 2019), 2000.

Vickery, K. J., Eckardt, F. D. and Bryant, R. G.: A sub-basin scale dust plume source frequency inventory for southern Africa, 2005-2008, Geophys. Res. Lett., 40(19), 5274–5279, doi:10.1002/grl.50968, 2013.

Winker, D. M., Hunt, W. H. and McGill, M. J.: Initial performance assessment of CALIOP, Geophys. Res. Lett., 34(19), L19803, doi:10.1029/2007GL030135, 2007.

Yorks, J. E., McGill, M. J., Palm, S. P., Hlavka, D. L., Selmer, P. A., Nowottnick, E. P., Vaughan, M. A., Rodier, S. D. and Hart, W. D.: An overview of the CATS level 1 processing algorithms and data products, Geophys. Res. Lett., 43(9), 4632–4639, doi:10.1002/2016GL068006, 2016.

https://doi.org/10.5194/acp-2019-507
Preprint. Discussion started: 3 June 2019

https://doi.org/10.5194/acp-2019-507
Preprint. Discussion started: 3 June 2019

Atmospheric Chemistry and Physics Discussions

Appendix A: Ground-based lidar analysis – link with spaceborne lidar observations

A.1 Description of the ground-based lidar

The ground-based lidar system used at the Henties Bay site is the ALS450® lidar manufactured by Leosphere and initially developed by the Commissariat à l'Energie Atomique (CEA) and the Centre National de la Recherche Scientifique (CNRS) (Royer et al., 2011a). The lidar emission is based on an Ultra® Nd:YAG laser manufactured by Quantel, delivering 6 ns width pulses at the repetition rate of 20 Hz with a mean pulse energy of 16 mJ at a wavelength of 355 nm. This system is particularly well-adapted to measure tropospheric aerosol profiles in the lower and middle troposphere. Its high vertical resolution of ~15 m after filtering and temporal resolution (~1 minute) gives the advantage of being able to follow the fast vertical evolutions of the atmospheric scattering layers and to accurately locate the aerosol layers within the troposphere. The lidar is composed of two receiver channels dedicated to the measurement of the co-polar and cross-polar signals. The detection is carried out by photomultiplier tubes and narrowband filters with a bandwidth of 0.5 nm. Its main characteristics are summarized in Table A1 where we have added the features of the LNG lidar for comparison.

Table A1: **Main characteristics of both the ALS and LNG lidars.**

	Ground-based lidar ALS	Airborne lidar LNG
Laser	Nd:YAG, flash-pumped, Q-switched Q-smart QUANTEL	Flashlamp-pumped Nd:YAG Q-switched oscillator (Quantel YG980)
Pulse duration	6 ns	6 ns @ 335 nm 7 ns @ 532 nm 8 ns @ 1064 nm
Reception channels	// 354.7 nm ⊥ 354.7 nm	// 355, 532 and 1064 nm ⊥ 355 nm
Emitted energy	16 mJ	50 mJ @ 335 nm 10 mJ @ 532 nm 50 mJ @ 1064 nm
Frequency	20 Hz	20 Hz
Reception diameter	15 cm	30 cm (Cassegrain telescope)
Field-of-view	~2.3 mrad	0.5 mrd @ 335 nm 6 mrd @ 532 nm 8 mrd @ 1064 nm
Filter bandwidth/transmission	0.5 nm / 70% @ 335 nm // and ⊥	5 nm/ 25% @ 335 nm // and ⊥ 0.2 nm / 25% @ 532 nm 1 nm / 30% @ 1064 nm
Detector	Photomultiplier (PM) tubes	PM Hamamatsu H6780-04 @ 355 nm

https://doi.org/10.5194/acp-2019-507
Preprint. Discussion started: 3 June 2019

		PM Hamamatsu H6780-02 @ 532 nm APD Perkin-Elmer C30659-1060 @ 1064 nm
Post processing vertical resolution	15-30	6 m

A.2 Calibration

In order to derive aerosol extinction coefficient profiles (AEC), the lidar apparent backscatter coefficient (ABC) measurements in the aerosol-free portions of the vertical profiles must be assessed and must follow the slope of the molecular backscattering. Furthermore, close to the lidar emission source the overlap factor generated by the overlap defects of the laser emission and telescope reception fields also needs to be assessed. The overlap factor is derived from measurements acquired in the horizontal line of sight, with the hypothesis of a homogeneous atmosphere along the line of sight between the emission and a distance of 1.5 km. The overlap factor and the associated standard deviation are shown in Figure A1. It can be considered that the correction of the overlap factor induces a relative error lower than 15% for an overlap factor between 0.8 and 1 (Chazette, 2003), corresponding to a distance of 150 m from the emitter. The molecular contribution is obtained from the ERA5 pressure and temperature data at the horizontal resolution of 0.25° using the Nicolet model (Nicolet, 1984). The error remains below 2-3% (Chazette et al., 2012b).

A representative sample of lidar profiles over the duration of the measurement field campaign is shown in Figure A2, showing the ABC profiles that correspond to the raw lidar signal corrected for both the contribution of the sky background and the solid angle, as in Royer et al. (2011a). The dates were chosen to be representative of the dataset of lidar vertical profiles encountered during the AEROCLO-sA campaign. The curves in black are the ABC profiles and those in red correspond to the molecular backscatter coefficient computed using ERA5 data. We note that in the top of the profiles there is a perfect coincidence that ensures that the lidar is well aligned. The area comprised between the black and red curves corresponds to the contribution of atmospheric aerosols and, in the upper part of the profiles, to that of optically thin clouds (Figure A2c and d). The aerosol content increases rapidly between 22 and 28 August, showing a significant evolution of aerosol contributions in the free troposphere (FT), between 1 and 5 km above the mean sea level (AMSL).

https://doi.org/10.5194/acp-2019-507
Preprint. Discussion started: 3 June 2019

Atmospheric Chemistry and Physics Discussions

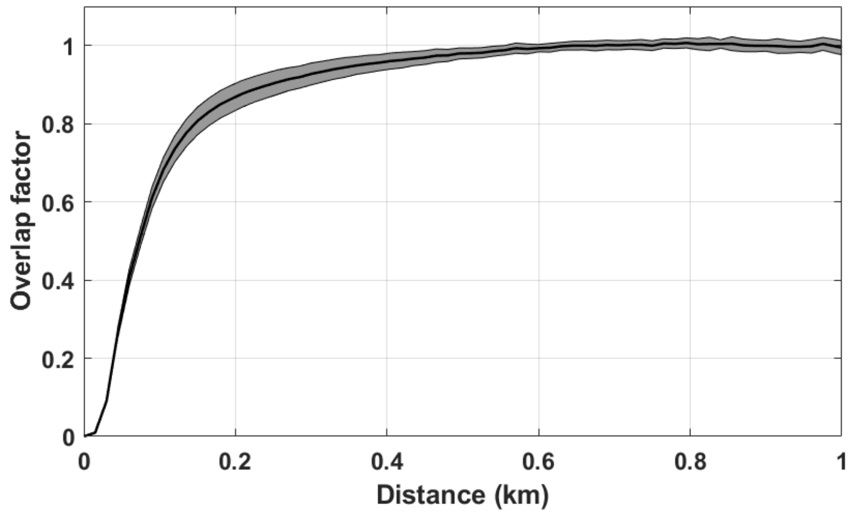

Figure A1: Overlap factor of the ALS (continuous black line) and its standard deviation (grey area).

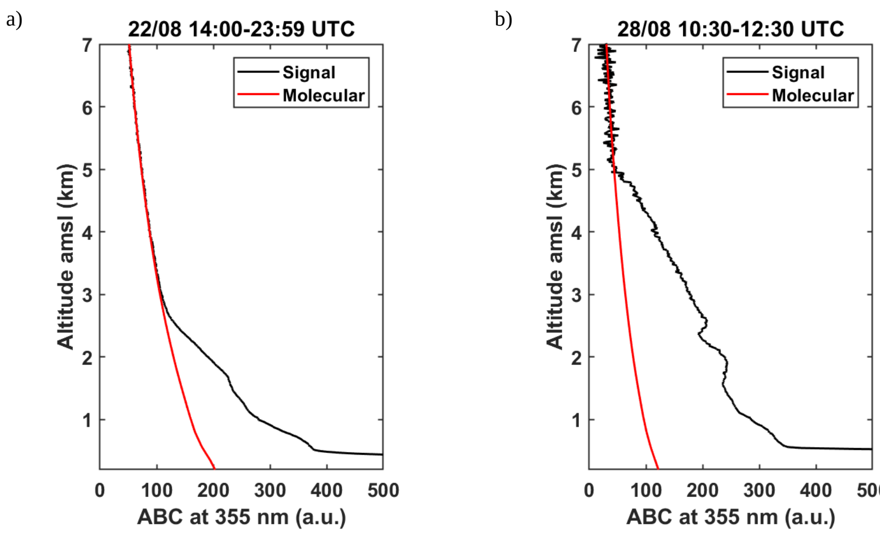

https://doi.org/10.5194/acp-2019-507
Preprint. Discussion started: 3 June 2019

Atmospheric Chemistry and Physics Discussions

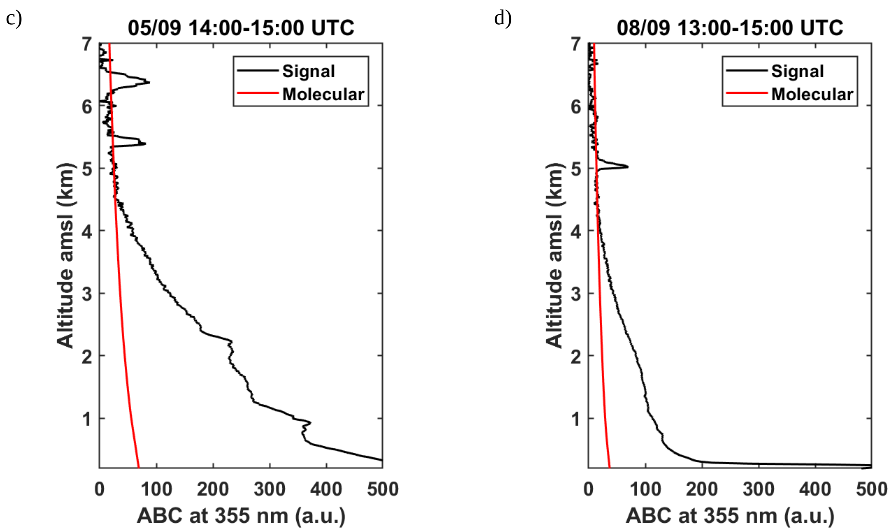

Figure A2: Apparent backscatter coefficient (black solid lines) profiles obtained from the ASL lidar in Henties Bay on: a) 22 August 2017 between 1400 and 2359 UTC, b) 28 August 2017 between 1030 and 1230 UTC, c) 5 September 2017 between 1400 and 1500 UTC, and d) 8 September 2017 between 1300 and 1500 UTC. The red lines correspond to the molecular backscatter coefficient computed using ERA5 data.

A.3 Ground-based lidar data processing using exogeneous constraints

The inversion procedure to retrieve the aerosol optical properties from ALS is well documented in previous articles where uncertainty sources are exhaustively quantified (e.g. Raut and Chazette, 2009; Royer et al., 2011b; Chazette et al., 2012a). In the present case, where a simple elastic backscattering lidar is used, we use additional constraints to the lidar equation using sun photometer-derived aerosol optical thickness (AOT) when available, but also the aerosol typing determined from the CALIOP and CATS measurements for cases where the orbit allowed the sampling of aerosols present in the FT. Figure A3 gives the example of the case of the geographical coincidence between the night CALIOP (CATS) orbit on 28 (30) August 2017 and the lidar measurements above the Henties Bay site. All available CALIOP and CATS orbits passing over Namibia were analysed and the results in terms of aerosol typing are given in Table 1 and Table 2. The correspondences in terms of LR are given in Table 2 for both instruments.

In the area of interest, aerosol properties are different in the planetary boundary layer (PBL), where the composition is dominated by marine and coastal dust emissions, and in the FT where the composition is dominated by long-range transport of BBA and dust emitted over the continental plateau. Therefore, we have used different values of LR in the PBL and in the FT to perform the lidar inversion when lidar measurements were acquired concomitantly with sun photometer AOT measurements. The LR in the FT is derived from the aerosol typing performed by the space-borne lidars (see Table 2). Values of 65-70±25 sr and 55±25 sr at 532 nm are used for the two main aerosol types sampled, namely smoke and polluted dust, respectively. The ground-based lidar in Henties Bay operates at 355 nm, the LR value is then different. Müller et al. (2007) showed that LR values at 355 and 532 nm differ by about of 20% for forest fire smoke and less than 10% for dust aerosols (see the Table 1 of their paper), widely included in the standard deviation of LRs derived from spaceborne lidars. In the PBL, the LR values are obtained via a minimization of the difference of AOT between the ground-based lidar and the sun photometer: the LR in

https://doi.org/10.5194/acp-2019-507
Preprint. Discussion started: 3 June 2019

Atmospheric Chemistry and Physics Discussions

the PBL is adjusted so that the AOT calculated from the lidar AEC profile matches best the AOT from the sun photometer. The LR values obtained during the field campaign are representative of clean marine air aerosols (i.e. 20-23 sr) and polluted dust (i.e. 55 sr) and coherent with the LRs from CALIOP for these aerosol types (compare Table 3 and Table 2). This was done for all days listed in Table 3, with the exception of 8 and 9 September 2017. On those days, the sun photometer AOT could not be used to constrain the inversion of the lidar measurements. This is likely due to the presence of unscreened clouds in the sun photometer inversion (as logged by the ground-based lidar on 8 September, Figure A2d). For those two days, we have used a LR of 20 sr in the PBL to be able to inverse the lidar data. Note that the use of a value of 55 sr in the PBL on those days (i.e. the value retrieved for the previous days) leads to an unrealistically high lidar-derived AOT. As a consequence, we observed an underestimation of the lidar-derived AOT when compared to the sun photometer level 2 product.

Besides the determination of the AEC, we also evaluated the linear particle depolarization ratio (PDR) values using an approach described in Chazette et al. (2012b). A detailed study of uncertainties for different aerosol types can be found in Dieudonné et al. (2017). Uncertainties of 2% on the PDR can be expected.

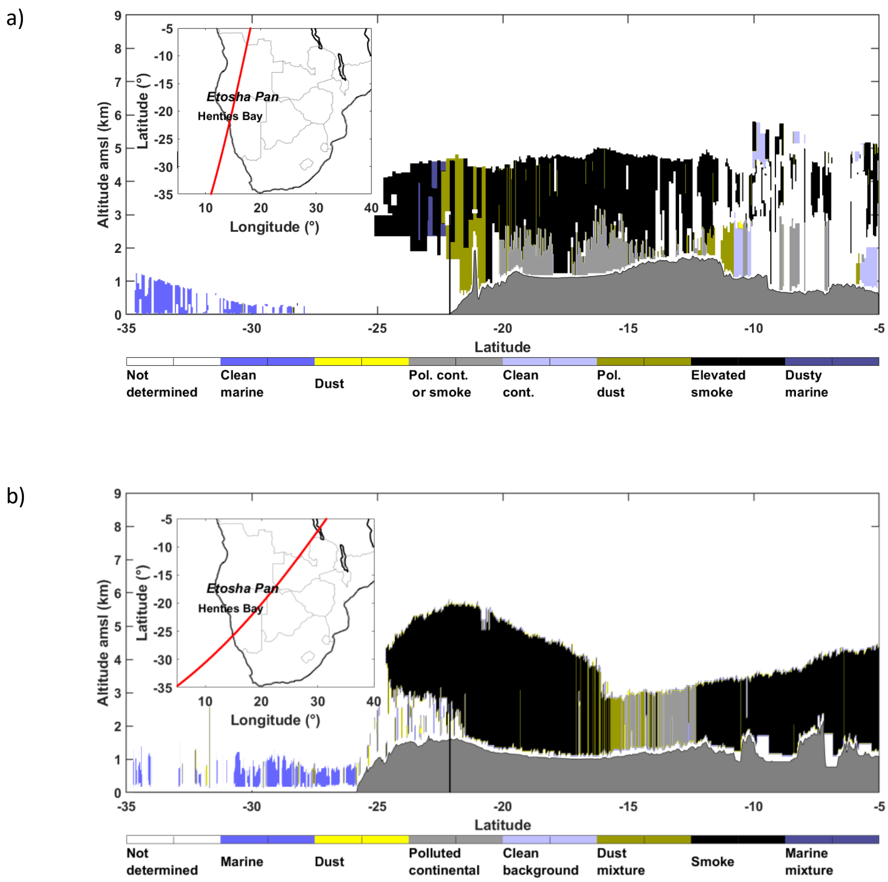

Figure A3: a) CALIOP-derived aerosol typing for the night time orbit (10.2017-08-28T00-08-17ZN) on 28 August 2017. b) CATS-derived aerosol typing for the night time orbit (2017-08-30T00-32-37T01-18-13UT) on 30 August 2017. The

https://doi.org/10.5194/acp-2019-507
Preprint. Discussion started: 3 June 2019

Atmospheric Chemistry and Physics Discussions

latitudinal location of the Henties Bay site is given by the vertical black line. Inserted panels in a) and b) show the position of the space-borne lidar tracks over southern Africa and with respect to Henties Bay.